



3D cell-printing of gradient multi-tissue interfaces for rotator cuff regeneration

Suhun Chae^{a,b,1}, Uijung Yong^{e,1}, Wonbin Park^a, Yoo-mi Choi^e, In-Ho Jeon^g, Homan Kang^d, Jinah Jang^{a,c,e,f}, Hak Soo Choi^{d,**}, Dong-Woo Cho^{a,c,*}

^a Department of Mechanical Engineering, Pohang University of Science and Technology, 77 Cheongam-ro, Nam-gu, Gyeongsangbuk-do, Pohang, 37673, South Korea

^b EDmicBio Inc., 111 Hoegi-ro, Dongdaemun-gu, Seoul 02445, South Korea

^c Institute for Convergence Research and Education in Advanced Technology, Yonsei University, 50 Yonsei-ro, Seodaemun-gu, Seoul, 03722, South Korea

^d Gordon Center for Medical Imaging, Department of Radiology, Massachusetts General Hospital & Harvard Medical School, 149 13th Street, Boston, MA, 02114, USA

^e Department of Convergence IT Engineering, Pohang University of Science and Technology, 77 Cheongam-ro, Nam-gu, Gyeongsangbuk-do, Pohang, 37673, South Korea

^f School of Interdisciplinary Bioscience and Bioengineering, Pohang University of Science and Technology, 77 Cheongam-ro, Nam-gu, Gyeongsangbuk-do, Pohang, 37673, South Korea

^g Department of Orthopaedic Surgery, Asan Medical Center, College of Medicine, University of Ulsan, 86 Asanbyeongwon-gil, Songpa-gu, Seoul, 05505, South Korea

ARTICLE INFO

Keywords:

3D cell-printing
Tissue-specific bioink
Gradient tissue scaffolds
Near-infrared fluorophores
Rotator cuff repair

ABSTRACT

Owing to the prevalence of rotator cuff (RC) injuries and suboptimal healing outcome, rapid and functional regeneration of the tendon–bone interface (TBI) after RC repair continues to be a major clinical challenge. Given the essential role of the RC in shoulder movement, the engineering of biomimetic multi-tissue constructs presents an opportunity for complex TBI reconstruction after RC repair. Here, we propose a gradient cell-laden multi-tissue construct combined with compositional gradient TBI-specific bioinks via 3D cell-printing technology. *In vitro* studies demonstrated the capability of a gradient scaffold system in zone-specific inducibility and multi-tissue formation mimicking TBI. The regenerative performance of the gradient scaffold on RC regeneration was determined using a rat RC repair model. In particular, we adopted nondestructive, consecutive, and tissue-targeted near-infrared fluorescence imaging to visualize the direct anatomical change and the intricate RC regeneration progression in real time *in vivo*. Furthermore, the 3D cell-printed implant promotes effective restoration of shoulder locomotion function and accelerates TBI healing *in vivo*. In summary, this study identifies the therapeutic contribution of cell-printed constructs towards functional RC regeneration, demonstrating the translational potential of biomimetic gradient constructs for the clinical repair of multi-tissue interfaces.

1. Introduction

Rotator cuff (RC) tears usually occur at the site of the fibrocartilaginous tendon–bone interface (TBI) as a result of trauma, overuse, or degeneration, which cause substantial pain and shoulder dysfunction [1]. Upon severe injury, the postoperative interface cannot heal completely owing to the avascular, acellular, and aneural nature of the TBI, resulting in disorganized and biomechanically inferior scar tissue formation. This poor tissue integration at the TBI after repair is strongly associated with the prevalence of re-tearing, high failure rates, and other

clinical complications [2,3]. In this regard, rapid and functional TBI regeneration after surgical intervention remains a critical challenge in clinical practice [3,4]. To address this issue, various approaches using multiphasic- or gradient-based scaffolds combined with the spatial control of cells, biomaterials, growth factors, and/or mineral contents have been attempted to recreate TBI gradients [1,3–8]. However, scaffolds developed thus far do not function adequately nor do they meet the requirements of TBI regeneration due to the low restoring potency of damaged fibrocartilage structures [9]. Therefore, it is highly desirable to develop functional multi-tissue constructs mimicking the gradual

Peer review under responsibility of KeAi Communications Co., Ltd.

* Corresponding author. Department of Mechanical Engineering, Pohang University of Science and Technology, 77 Cheongam-ro, Nam-gu, Pohang, 37673, Kyungbuk, South Korea.

** Corresponding author.

E-mail addresses: hchoi12@mg.harvard.edu (H.S. Choi), dwcho@postech.ac.kr (D.-W. Cho).

¹ These authors contributed equally to this work.

<https://doi.org/10.1016/j.bioactmat.2022.05.004>

Received 4 January 2022; Received in revised form 2 May 2022; Accepted 2 May 2022

2452-199X/© 2022 The Authors. Publishing services by Elsevier B.V. on behalf of KeAi Communications Co. Ltd. This is an open access article under the CC BY-NC-ND license (<http://creativecommons.org/licenses/by-nc-nd/4.0/>).

fibrocartilaginous transition of the TBI with structural integrity, consequently leading to functional RC regeneration.

To develop living multi-tissue constructs, bone marrow-derived mesenchymal stem cells (BMMSCs) have been widely used due to the high potency of differentiation into a multitude of mesodermal cell types [10], which promote tissue regeneration or the secretion of paracrine signals while maintaining immunomodulation properties after transplantation [10–12]. Several therapeutic approaches involving the application of BMMSCs have drawn increasing attention for RC repair [13–15], and biomaterial scaffolds with BMMSCs have shown regenerative potential with modest enhancements in the TBI healing outcomes [16,17]. However, it remains challenging to develop a cell-based tissue construct with the ability to reproduce the complex gradient features of the TBI; this is presumably due to the absence of biomimetic signaling with controlled guidance of regional MSC differentiation and extracellular matrix (ECM) deposition upon transplantation. Hence, to improve therapeutic efficacy, it is crucial to engineer a three-dimensional (3D) cellular scaffold with suitable instructive cues to restore the cell and matrix properties of heterogeneous TBIs.

Among various biofabrication techniques, 3D cell-printing has emerged as an innovative and powerful tool to create tissue analogs. 3D cell-printing enables versatile fabrication of living constructs by precisely layering printable inks comprising suitable biomaterials, functional cells, and bioactive molecules [12]. Because bioinks offer a favorable microenvironment for cellular activity [18], decellularized ECM (dECM) bioinks have recently been developed to modulate cellular functions [19,20] as well as to recapitulate the inherent microenvironment of native tissue, which together promote cell growth and differentiation into tissue-specific lineages with associated tissue function [21–25]. Numerous synthetic or natural biomaterials have been implemented to design functional scaffolds or injectable hydrogels, in order to enhance the bioactivity and regenerative capability for tissue engineering applications [26–28]. Despite the availability of several biofabrication strategies to develop bioscaffolds applied in the regeneration of multi-tissue interfaces, such as the tendon/ligament–bone interface and osteochondral interface, few studies have explored the 3D bioprinting-based approach to promote TBI healing for the treatment of RC injuries [25,29,30]. For instance, Jiang et al. [30] utilized 3D printing to fabricate multilayered polymeric scaffolds with cell-laden collagen-fibrin hydrogel for application in RC tendon regeneration, which resulted in supporting the tenogenic differentiation *in vitro* and showed enhanced mechanical properties and tissue biocompatibility *in vivo*. Moreover, in our previous study, a multiphasic 3D cell-printed TBI construct incorporating dECM bioinks derived from tendon and bone was constructed, which formed robust fibrocartilages at the regenerated interface and enhanced mechanical strength after RC repair [25]. However, it is still necessary to consider a more stringent TBI model to inherently recapitulate the natural graded physiology of heterogeneous populations of cells and ECM proteins as well as mineral contents. Moreover, the regenerative mechanism and functional role of *in vivo* transplanted tissue constructs have rarely been studied.

Near-infrared (NIR) fluorescence imaging has emerged as a promising tool for *in vivo* real-time monitoring transplanted cells, scaffold degradation, and tissue formation in the field of tissue engineering and regenerative medicine [31–34] due to its key advantages including negligible autofluorescence, minimized light scattering, and relatively low tissue absorption [35–37]. Despite the great advantage of NIR imaging, there have only been a limited number of tissue-specific fluorophores available in the field. Recently, we have reported a structure-inherent targeting (SIT) strategy to facilitate the development of tissue- and/or disease-specific NIR fluorophores. Armed with the SIT strategy, cartilage- and bone-targeted NIR fluorophores were developed which are no need for further conjugation with targeted agents but have a native targeting property [36,38]. Such connective tissue-specific fluorophores enable monitoring of the structural damage and disease progression in rheumatoid arthritis disease models

simultaneously in real-time using multispectral NIR imaging [37]. Typically, the RC injuries are not only confined to the ruptured site but also result in degenerative alterations to surrounding tissues, such as bone, tendon, and muscle [9]. Therefore, the nondestructive and consecutive real-time *in vivo* monitoring of the multi-tissue remodeling process in the regenerated area will potentially provide a better understanding of the regeneration capacity of the implanted construct for improved diagnosis and treatment of TBI injuries.

In this study, we aimed to delineate the functional assessment of 3D cell-printed multi-tissue constructs for RC regeneration in an irreparable chronic RC tear rat model (Fig. 1). To this end, we fabricated gradient multi-tissue interface constructs mimicking TBI specification using 3D cell-printing and tissue-specific dECM bioinks. These interface constructs possess similar gradient characteristics to native TBIs in terms of structural, compositional, and cellular heterogeneity, and their *in vivo* functionality was validated by 1) real-time monitoring of interface tissue formation and the regeneration process and 2) analysis of the walking gait and treatment efficacy. These 3D cell-printed constructs are advantageous in terms of reconstruction of the gradient interface and shoulder function recovery, which makes them promising for functional RC regeneration.

2. Materials and methods

2.1. Preparation of TBI-specific dECM bioinks

Porcine Achilles tendons supplied from a local slaughterhouse were administered with a succession of physical, chemical, and enzymatic treatment to produce tendon-derived dECM (TdECM) in accordance with our previous method with minor modifications [25]. The detail of preparing decellularized TdECM is available in the Supplementary data. Bone-derived dECMs (BdECMs) were prepared using the commercialized deCelluid (T&R Biofab, Korea) product made from porcine bone. To evaluate the remnant DNA contents after decellularization, 4',6-diamidino-2-phenyl-indole (DAPI) staining and double-stranded DNA quantification (dsDNA; DNA extraction kit, Invitrogen, USA) were performed for the natural and dECM tissues, as described previously [25, 39]. To prepare the dECM pre-gel solution, the desired amounts of TdECM and BdECM powder were weighed and digested in pepsin (10%, Sigma-Aldrich, USA) with acetic acid (0.5 M, Merck Millipore, USA) and hydrochloric acid (0.05 M, Merck Millipore, USA) for 4–5 d, respectively. The acidic dECM solution was neutralized using sodium hydroxide solution (10 M, Samchun Chemical, South Korea) before use. The final concentrations of the TdECM and BdECM bioinks were 20 and 40 mg/ml, respectively.

2.2. Cell isolation and expansion

Human BMMSCs (hBMMSCs; Catholic MASTER Cells, passage 2) isolated from the iliac crest of a male donor (age: 25 years) were obtained from the Catholic Institute of Cell Therapy (CIC; Seoul, Korea) with Institutional Review Board approval (Seoul St. Mary's Hospital, approval number PIRB-2018-E083). The cells were expanded in low glucose Dulbecco's Modified Eagle's Medium (DMEM; Hyclone, USA) supplemented with 20% fetal bovine serum (FBS; Hyclone, USA) and 1% penicillin/streptomycin (P/S; Hyclone, USA) at 37 °C in a 5% CO₂ atmosphere. The culture medium was replaced twice per week. All experiments were performed with cells of passage 4–5.

2.3. 3D cell-printing of multi-tissue construct mimicking TBI

All constructs were fabricated using our integrated composite tissue/organ building system [22,25,40]. This system constitutes six dispensing heads, a pneumatic pressure controller, a printing stage, and a temperature controller. Before printing, the composite polyurethane/poly-caprolactone (PU/PCL) polymer was prepared by

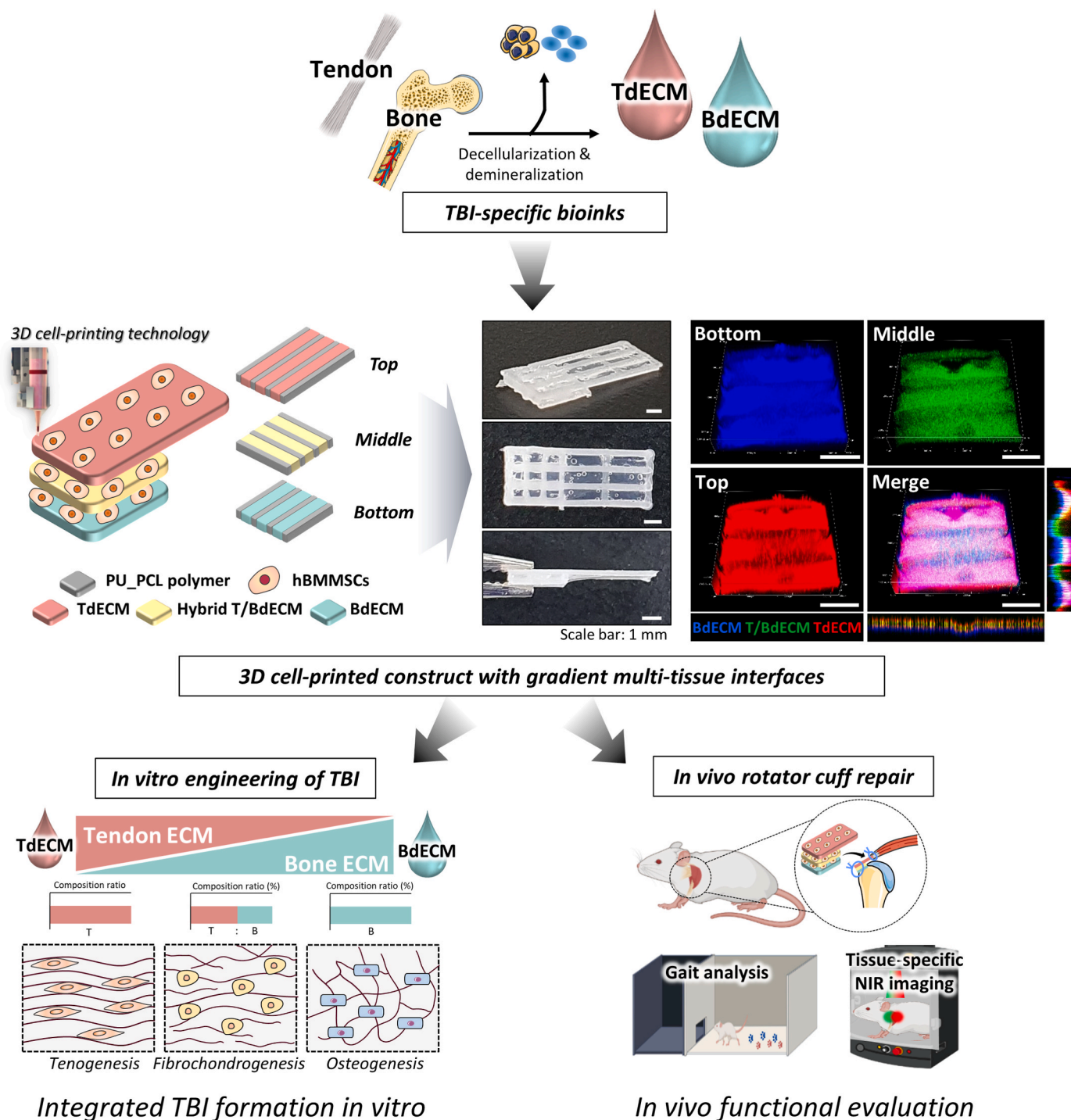


Fig. 1. Schematic outline of current research. This study developed a new therapeutic strategy for functional rotator cuff (RC) regeneration using 3D cell-printing and TBI-specific decellularized extracellular matrix bioinks. 3D cell-printed multi-tissue interface constructs with gradient structures were fabricated and evaluated their functionality, which showed integrated fibrocartilaginous gradient matrix formation *in vitro* and promoted graded interface tissue regeneration and improved shoulder locomotion function through implantation in a translational rat model. Thus, the therapeutic contribution of cell-printed construct towards functional RC regeneration was demonstrated.

the physical mixing of thermoplastic medical-grade PU (Carbothane PC-3575 A, Lubrizol, USA) and PCL (MW 43 000–50 000, Polysciences, USA) at a weight fraction of PU/PCL = 60/40; this ratio was selected based on a systematic characterization of the various weight ratios of the PU/PCL mixture (pure PCL, 20/80, 40/60, 60/40, 80/20, and pure PU) possessing the elastomeric property and an acceptable range of the melting temperature for extrusion (Fig. S1). The mixture was loaded into a steel syringe connected to a 200- μ m metal nozzle and heated to a

molten state at 190 °C during the printing process. The three dECM bioinks (TdECM, hybrid T/BdECM, and BdECM) containing hBMMSCs (density of 5×10^6 cells/ml) were separately transferred into a sterilized plastic syringe. For the *in vitro* analysis, stratified multiphasic TBI constructs were created using PU/PCL and the cell-laden bioinks. First, molten PU/PCL was extruded to fabricate the framework for structural integrity. To recapitulate the structural orientations at the native TBI, lattice (bone and fibrocartilage zones) and aligned (tendon zone)

patterns were fabricated with different sizes of the microchannels, which varied gradually from 300 to 750 μm throughout the stratified scaffolds. Next, appropriate cell-laden bioinks (TdECM, hybrid T/BdECM, and BdECM) were selectively deposited into the corresponding phase between the PU/PCL interlaid strands. These procedures were repeated layer-by-layer until a thickness of 1 mm was obtained. The dimensions of the constructs were $8 \times 3 \times 1 \text{ mm}^3$. For the *in vivo* studies, three-layered TBI scaffolds with the same dimensions were used, whereas three different cell-laden bioinks were stacked along the z-axis to form different layers (Fig. S2). Similarly, PU/PCL was printed to fabricate a physical support structure for the scaffolds, generating interlaid strands and interconnecting microchannels, which were alternatively filled with the appropriate cell-laden bioink (TdECM in the top layer, hybrid T/BdECM in the middle layer, and BdECM in the bottom layer for the tendon, fibrocartilage, and bone regions, respectively). In the PU/PCL framework, a strand diameter of 200–250 μm , strand width of 400–600 μm , and layer thickness of 300–350 μm were maintained during the printing process. These processes were repeated, and the structure was rotated by 90° for every 350 μm layer until a thickness of 1 mm was obtained. The 3D cell-printed constructs were incubated immediately after the printing process at 37 °C for 30 min to induce bioink gelation. After crosslinking, the culture medium were provided and the cultured constructs were employed in the *in vitro* and *in vivo* experiments.

2.4. Dual-channel fluorescence imaging system and NIR fluorophores

NIR fluorescence imaging was performed using a custom-built dual-NIR channel imaging system, which equipped with 660 nm excitation light (1.1 mW/cm²), 760 nm excitation light (4.2 mW/cm²), and 400–650 nm white light at 6000 lux (Fig. S3). With the choice of either 700 or 800 nm fluorescence images, color and NIR fluorescence images were collected simultaneously using custom software at rates of up to 15 Hz, while the field of view was manually adjusted using a NIKKOR 16–85 mm zoom lens (Nikon, Tokyo, Japan). To obtain merged color-NIR images, red and green pseudo-colors were used for the 700 nm and 800 nm channels, respectively. The imaging head was positioned at a distance of 249 mm from the surgical bed, and all NIR fluorescence images were captured under identical exposure times and normalizations. For NIR fluorophores, the 800-nm NIR fluorescence emitting C800–OMe and 700-nm NIR fluorescence emitting P700SO3 were synthesized as described previously [36–38]. They were dissolved in dimethyl sulfoxide to make $10 \times 10^{-3} \text{ M}$ stock solutions and stored at 4 °C until needed.

2.5. *In vitro* biological evaluation of hybrid bioinks on fibrochondrogenesis

To determine the optimized fibrochondrogenic bioink, we prepared hybrid bioinks by combining TdECM and BdECM at various volume ratios. The compositional designs of these hybrid bioinks are listed in Table S1, and these five types of hybrid bioinks (pure TdECM (10T), 7T/3B, 5T/5B, 3T/7B, and pure BdECM (10B)) were tested. The printed constructs of each hBMSCs-laden hybrid bioink (density of 5×10^6 cells/ml) were cultured in 24-well plates with chondrogenic induction supplements containing 1X insulin–transferrin–selenium (ITS; Gibco, USA), 100 nM dexamethasone (Sigma-Aldrich, USA), 50 $\mu\text{g}/\text{ml}$ ascorbate-2-phosphate (Sigma-Aldrich, USA), and 10 ng/ml transforming growth factor-beta1 (TGF- β 1; BD Biosciences, USA). After 14 d in culture, the fibrochondrogenic inducibility of each dECM bioink was studied through several experiments, including NIR fluorescence imaging, quantitative real-time polymerase chain reaction (qRT-PCR), and immunofluorescence (IF) staining. For the NIR fluorescence imaging analysis, cell-laden constructs were washed thrice with phosphate-buffered saline (PBS) and incubated with 2 μM of C800–OMe (cartilage-specific NIR fluorophores) at 37 °C for 2 h [36,37], followed by washing

thoroughly with PBS to remove unlabeled NIR fluorophores. The NIR fluorescence images were captured using the 800-nm channel. The SBR was determined by quantifying the fluorescence and background intensity of a region of interest (ROI) over each construct; specifically, it was calculated as $\text{SBR} = \text{fluorescence}/\text{background}$ (background = signal intensity of the blank area outside of the constructs; $n = 6$ per group). To confirm the NIR imaging observations and identify the effect of the optimal hybrid bioink on fibrochondrogenic differentiation, qRT-PCR analysis was conducted by examining the expression of related genes at the mRNA level. Changes in the expression of target genes were quantified using RT-PCR and compared with the mRNA level of the 10T. The primer sequences are listed in Table S2. Further, IF staining was performed to determine the production of fibrochondrogenic-specific proteins using anti-type-I collagen (1:200; GTX 41286, GeneTex), anti-type-2 collagen (1:200; MA5-12789, Invitrogen). The details of qRT-PCR analysis and IF staining are available in the Supplementary data.

2.6. *In vitro* engineered TBI model and characterization

Upon optimization of the fibrochondrogenic bioink, the integrated *in vitro* TBI model was designed and constructed using three types of cell-laden bioinks (TdECM, hybrid T/BdECM, and BdECM). Stratified multiphasic TBI constructs were fabricated through 3D cell-printing technique to engineer the tendon–fibrocartilage–bone (TFCB) *in vitro* model, as explained above. The TFCB *in vitro* model ($8 \times 3 \times 1 \text{ mm}^3$) composed of three single-phasic structures was fabricated using TdECM (tendon phase; 3 mm in length), hybrid T/BdECM (fibrocartilage phase; 2 mm in length), and BdECM (bone phase; 3 mm in length) bioinks, which were integrated through the printed PU/PCL framework. For comparison, a tendon–bone (TB) *in vitro* model composed of two single-phasic structures ($8 \times 3 \times 1 \text{ mm}^3$; 4 mm in length for each phase) was created using TdECM and BdECM bioinks as a control. After crosslinking for 30 min at 37 °C, the constructs were cultured in media containing a 1:1:1 mixture of tenogenesis supplement (100 $\mu\text{g}/\text{ml}$ ascorbic acid), chondrogenesis supplement (0.1 μM dexamethasone, 50 $\mu\text{g}/\text{ml}$ ascorbic acid, 1X ITS solution, and 10 $\mu\text{g}/\text{ml}$ TGF- β 1), and osteogenesis supplement (10 nM dexamethasone, 50 $\mu\text{g}/\text{ml}$ ascorbic acid, and 10 mM β -glycerophosphate (Sigma Aldrich, USA). The media were replaced twice per week for 14 d. To initially observe multi-tissue formation, NIR fluorescence imaging analysis was performed. Briefly, cultured constructs were subjected to double-labeling with 2 μM of C800–OMe (cartilage-specific NIR fluorophores) and P700SO3 (bone-specific NIR fluorophores) at 37 °C for 2 h [36–38], followed by washing twice with PBS to remove untagged NIR fluorophores. The macro-NIR fluorescence images were captured using a dual-channel intraoperative imaging system equipped with 700- and 800-nm channels. The SBR of each fluorescence signal at different zones was calculated for quantification as explained above ($n = 6$ per group). To further characterize the reconstructed TBI gradient and directed regional MSC differentiation capability, the TBI-relevant ECM distribution and mineralization were analyzed by qRT-PCR and IF staining. For the qRT-PCR analysis, samples at representative positions on TBI constructs (Z1: 1 mm, Z2: 4 mm, and Z3: 7 mm) were collected and the expressions of tenogenesis, fibrochondrogenesis, and osteogenesis were evaluated on samples from different zones, respectively. The specific primers for the target genes are listed in Table S2. For the IF assay, fluorescence images from different zones of constructs were obtained using the following primary antibodies: anti-type-I collagen (1:200), anti-type-II collagen (1:200), anti-aggrecan (1:100; AGC, ab3778, Abcam), anti-scleraxis (1:200; SCX, ab58655, Abcam), anti-Sex-determining region Y-box 9 (1:200; SOX-9, MA5-17177, Invitrogen), anti-tenomodulin (1:200; TNMD, ab203676, Abcam), anti-Runt-related transcription factor 2 (1:300; RUNX2, ab23981, Abcam). To confirm TBI-specific ECM proteins distribution and differentiation at different position of the constructs, the intensities of type-I and –II collagens, and AGC and the numbers of cells with

positive Scx and Sox9 signals were quantified and compared using the Image J software. To evaluate the mechanical properties of TFCB scaffolds ($3 \times 3 \times 0.6 \text{ mm}^3$; $n = 4$ per group), uniaxial tensile load was applied using a universal testing machine (Instron 4505, USA) with a strain rate of 0.1 mm/s.

2.7. Animal model and surgical procedure

All animal experiments were approved by Institutional Animal Care and Use Committee of Pohang University of Science and Technology (IACUC number: POSTECH-2021-0008) and were performed according to the guidelines recommended by these committees. Sprague–Dawley rats (male, 10 weeks old; OrientBio Inc., South Korea) were anesthetized using ketamine and xylazine. Under anesthesia, each rat's arm was externally rotated to identify the deltoid and underlying acromion, and a longitudinal 3-cm incision was made on the anterolateral aspect of the shoulder. The deltoid muscle was split to expose the supraspinatus tendon. The supraspinatus tendon was completely detached from its insertion at the greater tuberosity, and fibrocartilaginous tissues were completely scraped by a scalpel blade. To prevent spontaneous healing and reattachment, a drainage tube was used at the tendon insertion site to block direct contact between the tendon and bone (Fig. S4A). After 4 weeks, the animals that underwent chronic RC tears were subsequently subjected to repair. The operated rats were randomized into three experimental groups ($n = 10$ per group, total 30 animals): no implants (CTRL group), 3D bioprinted construct implantation (3DP group), and 3D cell-printed construct with BMMSCs implantation (3DCP group). For the CTRL group, the degenerative tendons were resected and partially reattached to the far lateral end of the greater tuberosity owing to severe supraspinatus tendon retraction. For the implantation groups, suited 3D scaffolds (3DP or 3DCP; $8 \times 3 \times 1 \text{ mm}^3$) were placed between the tendon end and greater tuberosity and fixed with a 4–0 Prolene suture (Fig. S4B). Following implantation, the wound was closed with sutures. To prevent the immune-rejection of the human cell-laden graft, all rats were immunized by daily administration with cyclosporine A (5 mg/kg), azathioprine (2 mg/kg), and methylprednisolone (2 mg/kg) [23]. After operation, all rats were returned to cages and supplied with ad libitum food and water until they were sacrificed at 12 weeks post-operation. Another 10 non-operated, age-matched healthy rats were used as normal group. At predefined time points (4, 8, and 12 weeks post-operation), each rat underwent gait analysis, *in vivo* NIR fluorescence imaging, and histological and biomechanical analyses. *In vivo* investigations were performed in a blinded fashion. An overall flowchart of the animal study is shown in Fig. S5.

2.8. Gait analysis for *in vivo* shoulder function assessment

The gait analysis was conducted to assess the repaired RC shoulder function, as previously described [41,42], at predetermined time points (4, 8, and 12 weeks after repair). A custom designed walking track system (length \times width \times height = $1200 \times 200 \times 160 \text{ mm}^3$) built from clear and black acrylic panels was used for functional testing. Prior to testing, the left forepaw (repair site) of each rat was colored blue and the right forepaw (intact site) was colored red with non-toxic washable ink. The rats were then allowed to comfortably walk on white paper strips along the confined walking track (Fig. S6A). The recorded pawprints were scanned and relevant gait parameters, including spatial parameters (stride length, stride width, and step length) and paw parameters (paw length and toe-spread) were analyzed. The asymmetry index (AI) was calculated to determine the level of asymmetry between repaired and intact sites using the formula $\text{AI} = (\text{NS} - \text{ES}) / 0.5 \times (\text{NS} + \text{ES}) \times 100$, where NS is a measured absolute value on the intact side and ES is a measured absolute value on the repaired side [42]. The detailed information and measuring methods are depicted in Fig. S6. For statistical comparison, the average of four steps was used in each case.

2.9. *In vivo* NIR fluorescence imaging

The P700SO3 and C800–OMe injection solutions were prepared in saline at specific concentrations as follows. At certain time points (4, 8, and 12 weeks after operation), P700SO3 (700 nm NIR, 100 nmol per rat) and C800–OMe (800 nm NIR, 200 nmol per rat) were intravenously injected into the operated rats via the dorsal penis vein 8 h and 4 h prior to imaging, respectively. At least 4 animals were analyzed and the NIR fluorescence signals from the rats were monitored in real-time at each time point. After shaving, a small incision on the overlying skin and deltoid muscle was made to expose the supraspinatus tendon and its insertion without destructing the anatomical structure. *In vivo* NIR imaging was performed with the dual-NIR channel imaging system equipped with 700- and 800-nm NIR channels, as described previously [37], while the rats were anesthetized throughout the imaging analysis. All experiments were conducted under aseptic conditions and the NIR images were captured under identical camera exposure times and image normalization (Fig. S7). After *in vivo* imaging, antibiotic injections were administered to the rats for infection prevention. To quantify the signal intensity and its distribution in the supraspinatus tendon–bone complex, the SBR was calculated using the fluorescence intensity versus the background signal of the neighboring tissues, such as muscle or skin, acquired over the imaging time frame.

2.10. Histological and IF analysis for *in vivo* evaluation

After implantation for 12 weeks, the rats were euthanized and the regenerated RCs were processed for histological examination by hematoxylin–eosin (HE), picrosirius red (PR), and safranin O (SO). The specimens ($n = 5$ per group) were fixed, demineralized, and embedded in paraffin wax. Sections were sliced at 5 μm thickness and then stained with HE, PR, and SO, as per the manufacturer's protocol. To validate the quality of the repaired tendons and their interface, the modified histological scoring system (Table S3) was applied according to a previous study [25,43]. According to the SO staining, to analyze the amount of neo-fibrocartilage interface (known as metachromasia), the red stained area was calculated against a green background at the TBI using Image J software. For IF staining, paraffin sections were dewaxed, followed by permeabilization with 0.1% Triton X-100 for 20 min and blocking with 5% BSA for 1 h. After that, sections were incubated with anti-human nuclear antigen (1:100; HuNu, MAB1281, Sigma-Aldrich) overnight at 4 °C to detect host tissue integration in cell-printed implants, followed by labeling with Alexa Fluor secondary antibody for 1 h and counter-staining with DAPI mounting medium.

2.11. Biomechanical evaluation of *in vivo* regenerated TBI

The biomechanical properties of the regenerated TBI complexes were evaluated using an Instron 4505 machine as per our prior methodology [22,25,39]. At 12 weeks post-operation, the humerus-supraspinatus tendon complex specimens were collected for all groups ($n = 4$ per group), and the normal supraspinatus tendon complexes were used as a control. Prior to testing, all extraneous tissues were discarded except for the supraspinatus tendon and its insertion. The cross-sectional areas of the TBIs were measured using digital calipers. The proximal humeral head was directly clamped through a screw-grip device of the mechanical testing machine. The supraspinatus tendon swathed in gauze was prepared to avoid slippage during testing, and then it was firmly fixed through the longitudinal axis of the humerus to allow tensile loads to be imposed along the anatomical direction. After applying a preload of 0.2 N, each specimen was pulled until failure with a constant rate of 0.1 mm/s [22,25]. Stress–strain curves were then plotted according to the collected load-displacement data, and the biomechanical properties of supraspinatus tendon–humerus complexes were calculated, including ultimate load to failure, elastic modulus, and ultimate stress.

2.12. Statistical analysis

Data were collected from at least biologically three independent experiments and are reported as mean \pm standard error of the mean. Using GraphPad Prism 6 (GraphPad Software Inc., USA), all statistical analyses were performed assuming a normal sample distribution with equal variance. For statistical comparison, two-tailed Student's t-test was applied for comparisons between two groups, while one-way ANOVA and Tukey's post hoc test were performed for comparisons between more than three groups. Values of $p \leq 0.05$ were considered statistically significant.

3. Results and discussion

3.1. Optimization of bioink formulation for fibrochondrogenesis

We previously developed tissue-specific bioinks by decellularizing porcine tendon and bone tissues for engineering TBI and verified the chondro-inductive potential of their hybrid bioink containing TdECM and BdECM [25]. This result suggests that the co-existence of a TBI-specific environment with dECM bioinks could regulate the stem cell behavior to induce fibrocartilage formation mimicking the TBI. In the present study, TdECM and BdECM obtained from the porcine tissues were prepared using the decellularization method. Through quantitative and qualitative analyses, the cellular substances were significantly removed, and the remnant DNA contents of TdECM and BdECM were lower than 50 ng dsDNA/mg dry tissue, thus fulfilling the minimal requirements for decellularized materials [19,44]. This indicated that the adapted decellularized method was effective (Fig. S8). Based on this, to optimize the fibrochondrogenic bioink that can recapitulate the intermediate zone of the TBI, we set up an experimental design by blending

TdECM and BdECM at various volume ratios (Table S1). All hybrid bioinks encapsulating human BMMSCs (hBMMSCs) maintained high cell viability over 14 d, and the metabolic activities of living cells in all hybrid bioinks significantly increased up to 14 d of culturing, both indicating good compatibility and cell proliferation superiority regardless of the hybrid bioink combination (Fig. S9).

To evaluate the biological performance of encapsulated hBMMSCs under various hybrid bioink combinations, the fibrochondrogenic formation of printed constructs was observed by labeling with cartilage-targeting fluorophore (C800–Ome) (Fig. 2A). C800–Ome facilitates effective fibrocartilage-selective imaging via specific uptake in negatively charged glycosaminoglycan (GAG) and chondrocyte by the SIT manner [36]. At day 14, the NIR imaging results for all groups showed fluorescent signals from C800–Ome in the 800 nm channel, which represented in pseudo color by green. Notably, the 7T3B group (7:3 ratio of TdECM to BdECM bioinks) exhibited the highest fluorescent intensity among the groups, indicating remarkable fibrochondrogenic capacity of cell-laden constructs with 7T3B hybrid bioink (Fig. 2B). To ascertain the NIR imaging results, IF staining and gene expression analyses were further performed. IF staining confirmed that the 7T3B hybrid bioink induced fibrochondrogenic differentiation of hBMMSCs, yielding the largest amount of fibrocartilage matrix at day 14, as detected by type-I and –II collagen staining (Fig. 2A). Similarly, the expression of fibrochondrogenic genes (COL1A1 and COL2A1 mRNA) was significantly higher in the 7T3B group, than in the other groups, suggesting strong fibrochondrogenic mRNA phenotypes (Fig. 2C). TGF- β /bone morphogenetic protein (BMP) signaling is critical for fibrochondrogenesis and TBI development [45,46]. Accordingly, crosstalk between TGF- β and BMP signaling-related molecules in a particular blend of hybrid dECM bioink may be the potential driving force to fibrochondrogenic differentiation of hBMMSCs. There is a need for more in-depth analysis to

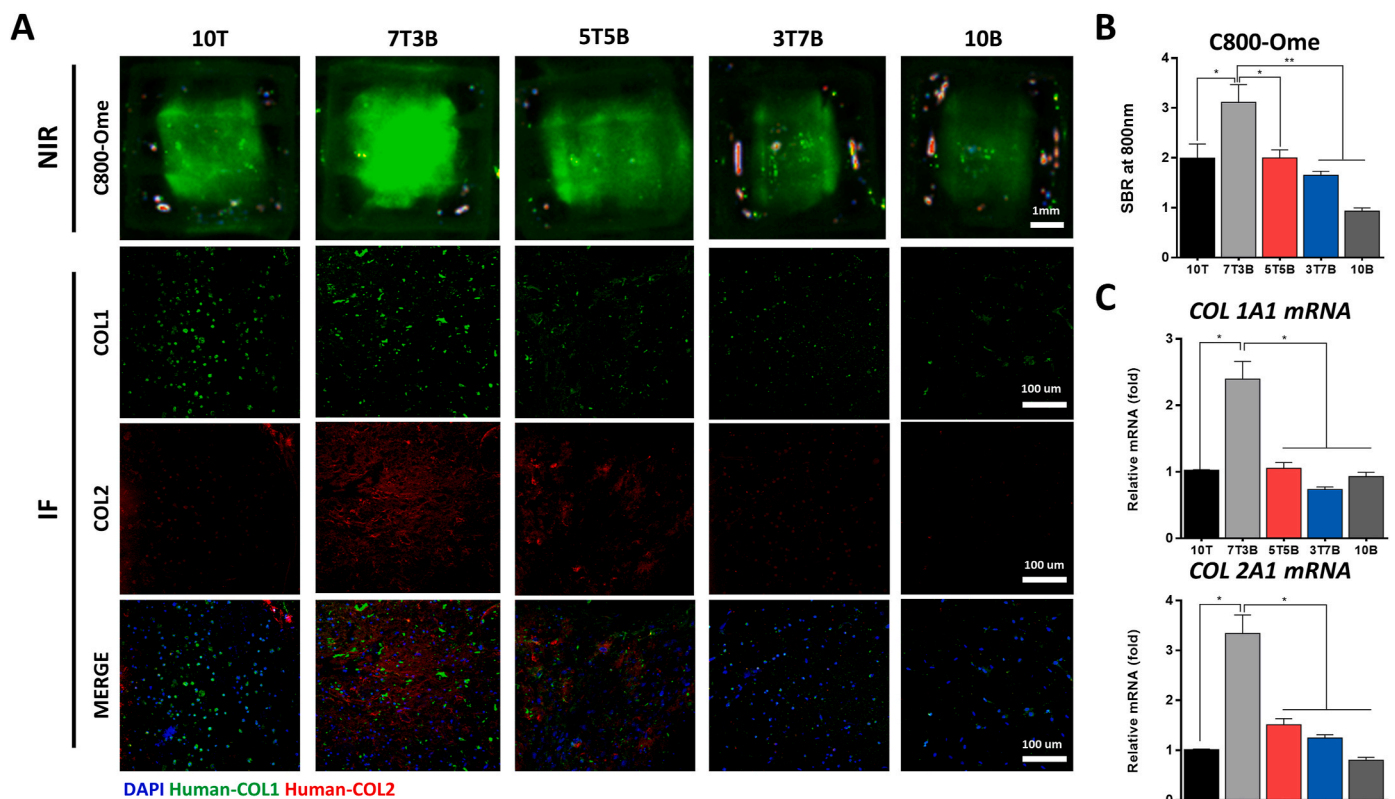


Fig. 2. Optimization of fibrochondrogenic bioink by combining TdECMs and BdECMs at various volume ratios. (A) Near-infrared (NIR) images and immunofluorescence staining of synthesized type-I (green) and –II (red) human collagens on various cell-laden tissue constructs at day 14. (B) Signal-to-Background Ratio (SBR) in the 800-nm channel ($n = 6$ per group). (C) qRT-PCR analysis of gene expression for COL1A1 and COL2A1 at day 14 ($n = 6$ per group; * $p < 0.05$ and ** $p < 0.01$).

understand precise mechanisms and involved signaling pathways on MSC differentiation according to a particular composition of tendon and bone dECMs. Overall, the results indicate that 7T3B group has the best potential to generate a fibrocartilage-like matrix *in vitro* in the cell-printed construct. Therefore, the 7T3B hybrid bioink was selected as the optimized fibrochondrogenic material for the following experiments.

3.2. Generation of *in vitro* TBI model with defined interface emulating fibrocartilaginous gradient matrix

Given the spatial gradients in the structure, composition, and cell phenotype of the TBI, the development of an integrated biomimetic TBI model for the reconstruction of this multi-tissue interface remains a current scientific challenge. A TBI complex involves three distinct but functionally integrated zones: tendon, bone, and their transitional fibrocartilage. Thus, complex anisotropic organization of the TBI is remarkably pertinent to the spatial biomechanics and load-transfer functions [47]. For compliance with biological appearance, the characteristic inhomogeneity of the TBI construct was achieved using 3D cell-printing and tissue-specific bioinks. To reflect the structural and compositional graduality, three types of bioinks (pure TdECM, pure BdECM, and 7T3B hybrid bioinks) were employed to fabricate multiphase tissue constructs. Considering anatomical features, each cell-laden bioink was precisely localized to a corresponding phase and merged through a polymeric framework, resulting in the successful fabrication of an integrated multiphase TBI construct (Fig. 3A and B).

The TB model was designed to organize two distinct phases representing the TdECM and BdECM bioink localizations to the tendon and bone regions, respectively (Fig. 3A). In contrast, the TFCB model containing three single phases (tendon, fibrocartilage, and bone regions) formed a seemingly continuous 3D tissue structure in which components of the TdECM and BdECM were discretely stratified along with inverse gradients to simulate native TBI layers (Fig. 3B). Fluorescent images facilitated visual inspection of the multiphase TdECM and BdECM patterning with hBMMSCs for the TB and TFCB models using green (within TdECM) and red (within BdECM) fluorescent beads (Fig. 3A and B). The multiphase distributions of tendon, bone, and their intermediate fibrocartilage zones were gradually observed in the triphasic TFCB model, whereas spatially distinguished tendon and bone regions were shown by the biphasic TB model. Quantified fluorescence intensity profiles confirmed a spatial distinction at the interface area in both TBI constructs. Furthermore, the TFCB constructs showed a greater overlap between green and red fluorescence (>30% overlap) than the TB constructs (8% overlap), indicating that the anisotropic and hierarchical structure in the TFCB model can better imitate the native fibrocartilaginous interface (Fig. 3A and B).

To identify the extent of TBI development and regional differentiation in the engineered tissue models, we investigated their gradient characteristics when cultured with hBMMSCs encapsulated in different types of bioinks. In combination with a dual-channel NIR imaging system, C800-OMe and P700SO3 NIR fluorophores were used to detect the specific uptake of the fibrocartilaginous matrix and mineralization of the *in vitro* engineered TBI constructs, respectively. In essence, C800-OMe

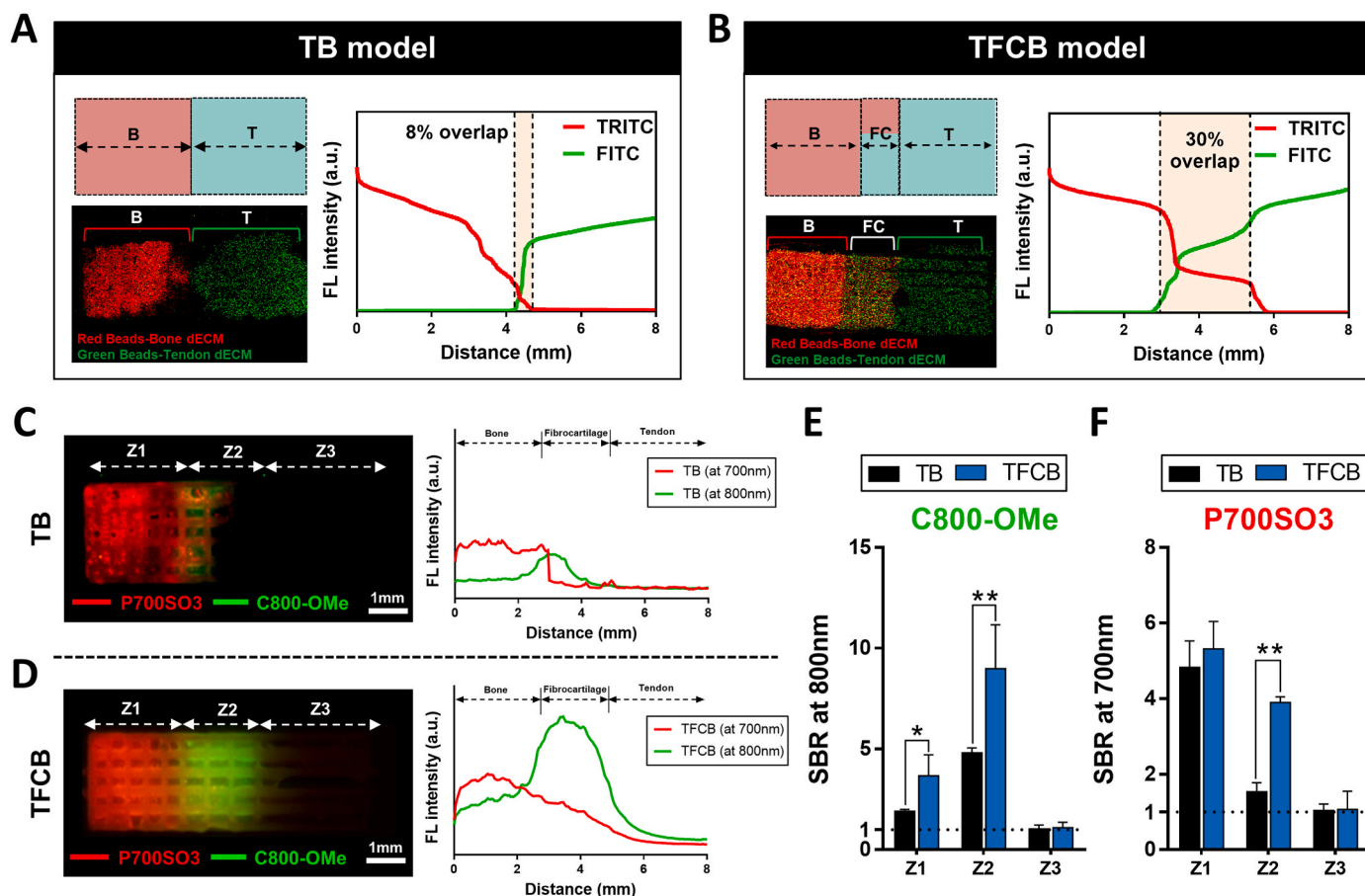


Fig. 3. *In vitro* engineering of tendon-bone interface (TBI) model via 3D cell-printing. (A and B) Schematic diagrams of *in vitro* engineered TBI model. Design and representative fluorescent image and its linear intensity profile of (A) biphasic TB model and (B) triphasic TFCB model. (C and D) NIR imaging of TBI model using C800-OMe and P700-SO3 after 14 d of culturing. Dual-channel imaging of TBI formation and mineralization, and line profiling graph of fluorescence intensity of the (C) TB and (D) TFCB models. (Z1: Bone zone; Z2: Fibrocartilage zone; Z3: Tendon zone). (E and F) SBR values of (E) C800-OMe and (F) P700SO3 at different zones in the 800-nm and 700-nm channels, respectively (n = 6 per group; *p < 0.05 and **p < 0.01).

reaches the fibrocartilage matrix through diffusion-based penetration and adheres to negatively charged glycosaminoglycans (GAG) and fibrochondrocytes via strong charge interactions enabling effective fibrocartilage-selective imaging [36]. P700S03 contains phosphonate groups within its chemical structure, and strongly binds to bone minerals such as hydroxyapatite (HA) and calcium phosphate (CP), enabling NIR imaging of bone minerals [38]. In other words, tissue-targeted NIR fluorophores provide a facile strategy to detect fibrocartilaginous and bone-like tissues in the *in vitro* engineered TBI constructs by the SIT manner [36–38]. Following 14 d of culturing, NIR images of the whole constructs were obtained in the 700 nm (red) and 800 nm (green) channels simultaneously (Fig. 3C and D). All tissue constructs revealed both C800–OMe and P700S03 signals in the fibrocartilage and bone phases, while they were rarely observed in the tendon phase, indicating the spatial distribution of the matrix and mineral components over the cell-printed constructs (Fig. 3C, D). During *in vitro* culture over 14 days, the hBMMSCs not only underwent zone-specific differentiation in the printed constructs but also produced matrix proteins, and thus induced multiphasic bone-fibrocartilage-tendon structure formation mimicking native TBI on day 14. Consequently, C800–OMe and P700S03 specific uptakes resulted from the production of fibrocartilaginous matrix (Z2) and minerals (Z1) in matured TBI constructs, respectively (Fig. 3C and D). In contrast, the NIR fluorophores did not bind to tendon regions due to the absence of target structures. Notably, in the TFCB construct, the highest fluorescent intensity of C800–OMe was shown in the middle, and its signal gradually decreased towards each end (Fig. 3D). This specificity was further confirmed by the intensity line profile and signal-to-background ratio (SBR) at 800 nm (Fig. 3E). In addition, the gradient in mineralization on the TFCB construct was clearly visualized,

representing a gradual slope in the intensity line profile of P700S03 and variation in the SBR at 700 nm (Fig. 3D, F); on the contrary, TB construct only presented very limited mineralization in the bone phase, with a faint slope and diminished fluorescence intensity (Fig. 3C, F). Consequently, the results indicated spatial differences in fibrocartilage matrix and mineral depositions within the multiphasic gradient TFCB construct.

To further clarify the ECM deposition and its spatial distribution in the TBI models, IF staining was performed. The TFCB constructs exhibited superior matrix heterogeneity and interface formation with controlled spatial distribution of structural protein compared to the TB constructs (Fig. 4A). At day 14, type-I collagen was synthesized by MSCs and distributed throughout the constructs, particularly in the bone and tendon phases of the TFCB constructs. Moreover, MSCs in the interphase concurrently produced abundant type I and II collagen, and aggrecan proteins in the TFCB constructs on day 14, suggesting that the TFCB model gave rise to fibrocartilaginous matrices in the transitional zone, unlike the TB model (Fig. 4A and B). These results agree well with the NIR-based molecular imaging analysis results that the integrated TFCB construct with inverse gradients generated a native-like fibrocartilaginous gradient interface (Fig. 3C–F and Fig. 4 A, B). Thus, our findings suggest that quantitative NIR-based molecular imaging can effectively decipher the multi-tissue formation of cell-printed constructs and can be a reliable tool for monitoring cellular activity and subsequent tissue development *in vitro*.

To examine the regional differential behaviors of hBMMSCs exhibited by the TB and TFCB models, the expression patterns of tenogenic (SCX, TNMD), chondrogenic (COL2A1, SOX 9) and osteogenic (RUNX2, osteocalcin (OCN)) differentiation markers were assessed by qRT-PCR

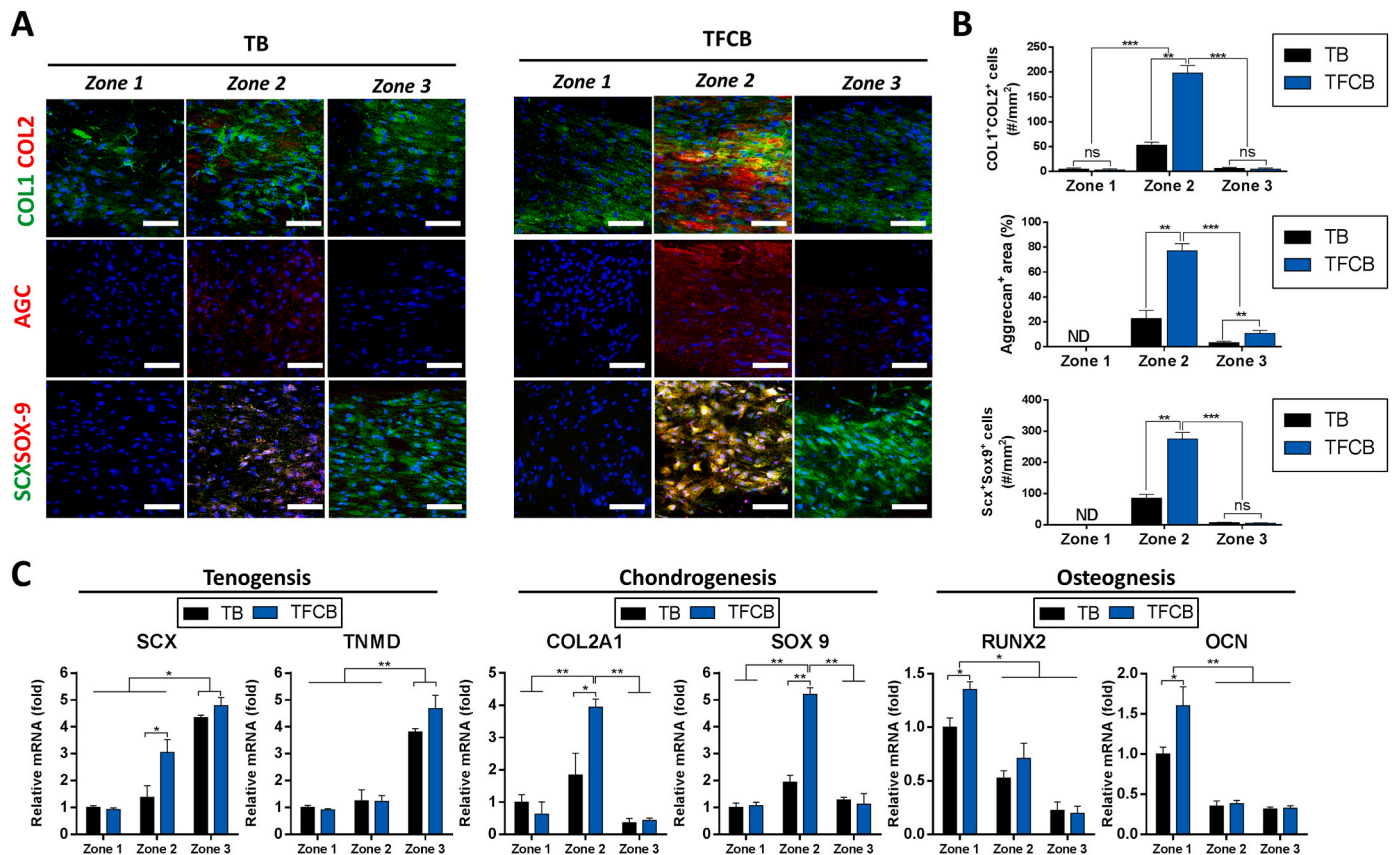


Fig. 4. Characterization of zone-specific tissue formation mimicking TBI. (A) Immunofluorescence staining of synthesized type-I and -II collagens and aggrecan as well as co-expression of Scx and Sox9 at different zones on day 14. Scale bar = 100 μ m. (B) Quantification of immunofluorescence staining for type-I and -II collagens, aggrecan, and Scx⁺/Sox9⁺ at different zones. (C) qRT-PCR analysis of hBMMSCs after culturing on the constructs for 14 d, including tenogenic, chondrogenic, and osteogenic differentiation markers at different zones (n = 6 per group; *p < 0.05, **p < 0.01, and ***p < 0.001).

after 14 d of culturing. The hBMMSCs co-cultured in the TFCB constructs exhibited significant upregulation of tenogenic, chondrogenic, and osteogenic gene expressions according to each corresponding zone, demonstrating the regional differences in MSC differentiation towards the three intended lineage traits (Fig. 4C). For instance, tenogenic genes were robustly expressed at the tendon zone where the TdECM bioink was predominant, and the gene expression patterns of the other two cases (chondrogenic and osteogenic genes) showed similar tendencies. These results were further supported by IF staining outcomes. In agreement with these results, the IF images showed that the TNMD protein was expressed the most in the tendon zone (zone 3) and the RUNX2 protein was expressed the most in the bone zone (zone 1) for both the TB and TFCB constructs after 14 d of culturing, suggesting the preferential differentiation of hBMMSCs into the tenogenic and osteogenic commitments in their corresponding zones (Fig. S10). The RT-PCR and IF results corroborate that the tenogenic and osteogenic differentiation process of the hBMMSCs was primarily affected by the localized tissue-specific bioink components (TdECM and BdECM bioinks, respectively). We also performed IF staining for Scx and Sox9 to investigate the potential mechanism of fibrochondrogenic differentiation in the middle zone of the tissue constructs (Fig. 4A). Notably, a greater number of Scx⁺/Sox9⁺ expressing cells, which are indicative of early progenitor cell markers crucial for TBI development, prevailed at the interphase of TFCB constructs (Fig. 4B). This corresponds with the PCR analysis of more upregulated Scx and Sox9 mRNA expressions in the interface region of TFCB constructs, compared to the TB control (Fig. 4C). In other words, an abundance of Scx⁺/Sox9⁺ progenitors in the transition zone may extensively contribute to strong fibrocartilage formation between tendon and bone. Several studies have identified specific markers essential for TBI development and maturation, including Scx, Sox9, and Gli1 [48–51]. It was previously reported that unique Scx⁺/Sox9⁺ stem/progenitors are specifically modulated by TGF- β /BMP signaling pathways, which functionally establish junction formation between tendon/ligament and bone [45,48,49]. In addition, the hedgehog signaling pathway is known to be a master regulator of endochondral formation and hedgehog-responsive Gli1-expressing cells primarily contribute to the mineralized fibrocartilage formation [50,51], which was not investigated in this study, but it is of interest for future research. Although the mechanisms of cellular and cell-matrix interactions as well as their key signaling pathways leading to native-like fibrocartilage interface formation remain unknown, it is probable that concurrent Scx and Sox9 expression as well as heterotypic cellular interaction at the interphase significantly contribute to fibrocartilaginous interface development and mineralization, resembling the gradient features of the native TBI. We believe that our gradient multi-tissue system incorporating tissue-specific bioinks and stem cells can provide a better understanding of the developmental mechanism as well as a scaffold design strategy for interface tissue engineering applications.

Additionally, the biomechanical properties of TFCB constructs cultured with hBMMSCs for 14 d (cellular TFCB) and the TFCB constructs without cells (acellular TFCB) were evaluated before *in vivo* implantation. The tensile properties of *in vitro* TFCB constructs were measured using a universal testing machine. The failure load and elastic modulus of the cellular TFCB gradually increased over time and showed 2.15 and 1.84 times higher than those of the acellular TFCB, respectively ($p < 0.01$) (Fig. S11). The results suggest the contribution of cell remodeling and ECM depositions within the scaffolds in improving the mechanical properties of the TFCB construct *in vitro*.

These findings collectively demonstrate that multi-tissue system containing spatially orchestrated dECM components with inverse gradients results in zonal differences in MSC differentiation behaviors, which are indicative of multicellular phenotypes as well as varying structural protein depositions in their respective regions. Thus, the cell-printed constructs with compositional inverse gradients of TBI-specific bioinks (TFCB model) are promising for achieving functional reconstruction of a multi-tissue transition at the TBI *in vivo*.

3.3. *In vivo* functional assessments of 3D cell-printed multi-tissue interface for RC repair

Gait analysis was conducted as the first step of *in vivo* functional evaluation after RC repair. Analysis of the walking patterns of experimental animals provides quantifiable behavioral data on how the given injury and repair impact the animal movements [41]. At certain time points (4, 8, and 12 weeks), rat pawprints were collected and used to comprehensively analyze gait parameters, including spatial parameters (stride length, stride width, and step length) and paw parameters (paw length and toe-spread) (Figs. S6 and S12 and Fig. 5A). The results confirmed gait abnormalities at the repair site for all groups at 4 weeks after surgery, as evidenced by the attenuated stride length and width as well as increased asymmetry of other parameters compared to those of normal rats (Fig. S12 and Fig. 5B and C). While all groups showed a trend towards recovery over time, the pawprints of the 3DP and 3DCP groups showed notable recovery from 4 weeks onwards, whereas the CTRL group showed only partial recovery (Fig. 5B and C). Notably, all gait parameters of the 3DCP group consistently improved at each time point. Furthermore, their values were rapidly ameliorated and eventually reached normal levels at 12 weeks post-operation, implying outstanding repair performance by the 3DCP implants (Fig. 5B and C). These results are further supported by video clips (Videos S1–S4); all animals that underwent operations seemingly resumed load bearing and locomotion as early as 4 weeks post-operation, and the rats in the 3DCP group could fully restore load bearing and locomotion with active and extensive movements at 12 weeks post-operation. Our findings suggest that gait analysis proves useful in quantitatively evaluating shoulder function by scoring behavioral phenotypes and is capable of detecting differences in degree of healing as well as functional enhancements for repaired animals. Thus, the above gait analyses clearly indicate enhanced shoulder function recovery after 3DCP implantation, which was close to normal conditions.

Supplementary video related to this article can be found at <https://doi.org/10.1016/j.bioactmat.2022.05.004>

Next, the progress of multi-tissue regeneration was monitored in the RC repaired rat model after intravenous injection of P700SO3 (700 nm NIR) and C800–OMe (800 nm NIR) to validate surgical outcomes (Fig. 6A). Based on our previous studies, the injected NIR fluorophores were cleared from the body within 24 h except for the target signals in the bones and cartilages [36,38]. The dual-channel NIR fluorescence imaging allowed an independent and direct *in vivo* assessment of the multi-tissue interface healing process in real time within a single animal model until 12 weeks after surgery (Fig. 6B and C). To determine the fibrocartilaginous interface regeneration, 800 nm fluorescent signals were quantified in the shoulders of RC repaired rats at each time point (Fig. 6C). In the control group (without implantation), fluorescence signals in the 800 nm channel at the repair site were almost undetectable (SBR <2) up to 12 weeks post-operation, suggesting unfavorable tendon–bone attachment (Fig. 6D). In contrast, both the 3DP and 3DCP groups showed strong fluorescence signals in their corresponding region at all-time points, and the NIR signals gradually increased over time, indicating fibrocartilage formation between supraspinatus tendon and bone after repair with the printed constructs (Fig. 6C). Comparatively, the 3DCP group displayed stronger fluorescence with enhanced SBR values compared with 3DP ($p < 0.05$) and CTRL groups ($p < 0.01$) at all-time points. Notably, the 3DCP group exhibited prominent fibrocartilage-specific signals at the healing site as early as 4 weeks post-operation, and the final SBR value at 12 weeks was 5.1. This fluorescence is comparable with the normal group, indicating a local deposition of fibrocartilage matrix at the healing site (Fig. 6D). Additionally, the degrees of bone regeneration were evaluated in the same rats with P700SO3 under the 700 nm channel, while the fibrocartilage was visualized with C800–OMe under the 800 nm channel (Fig. 6C, D, E). The bone-targeting agent of P700SO3 favorably binds to mineral contents in bone tissues (e.g., HA and CP) and exhibits direct uptake

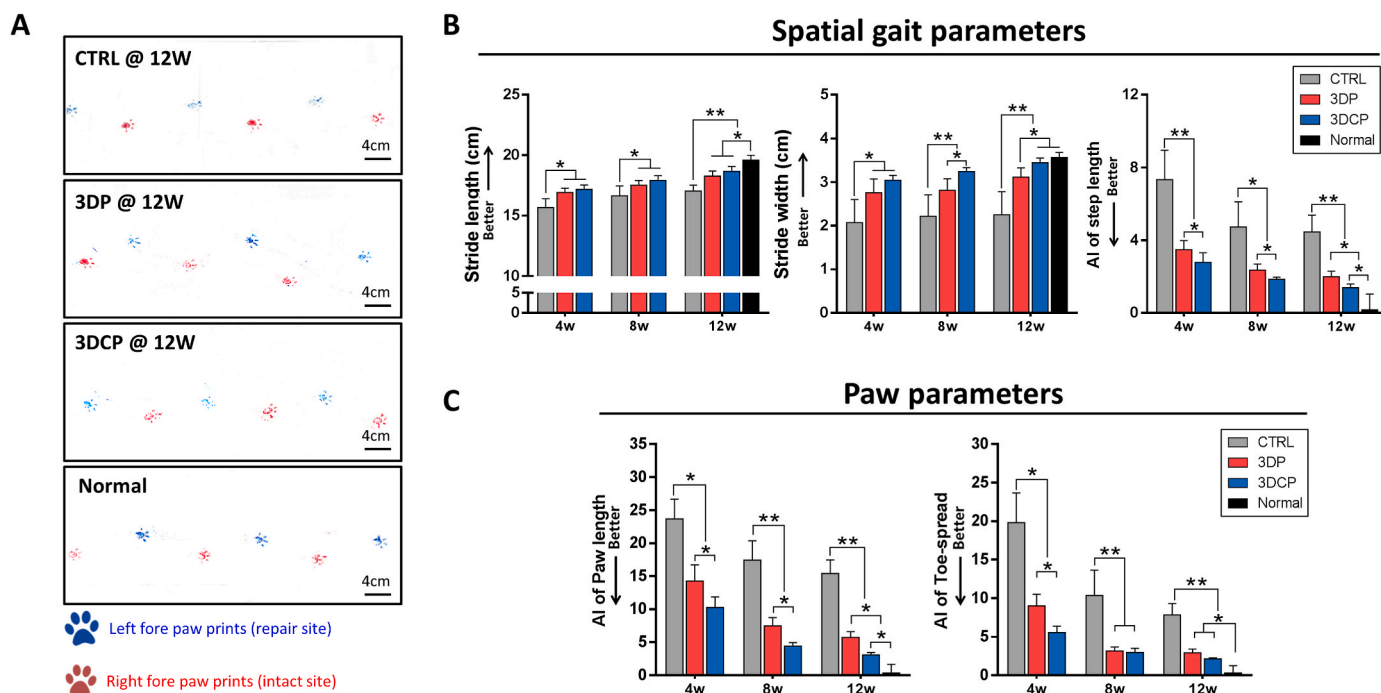


Fig. 5. Gait analysis results at 4, 8, and 12 weeks post-operation. (A) Representative pawprints of the CTRL, 3DP, and 3DCP groups at 12 weeks post-operation in comparison with the normal group. (B and C) Quantification of gait parameters at 4, 8, and 12 weeks post-operation (n = 4 per group). (B) Spatial gait parameters, including stride length, step length, and stride width, and (C) paw parameters, including paw length and toe-spread. (*p < 0.05 and **p < 0.01).

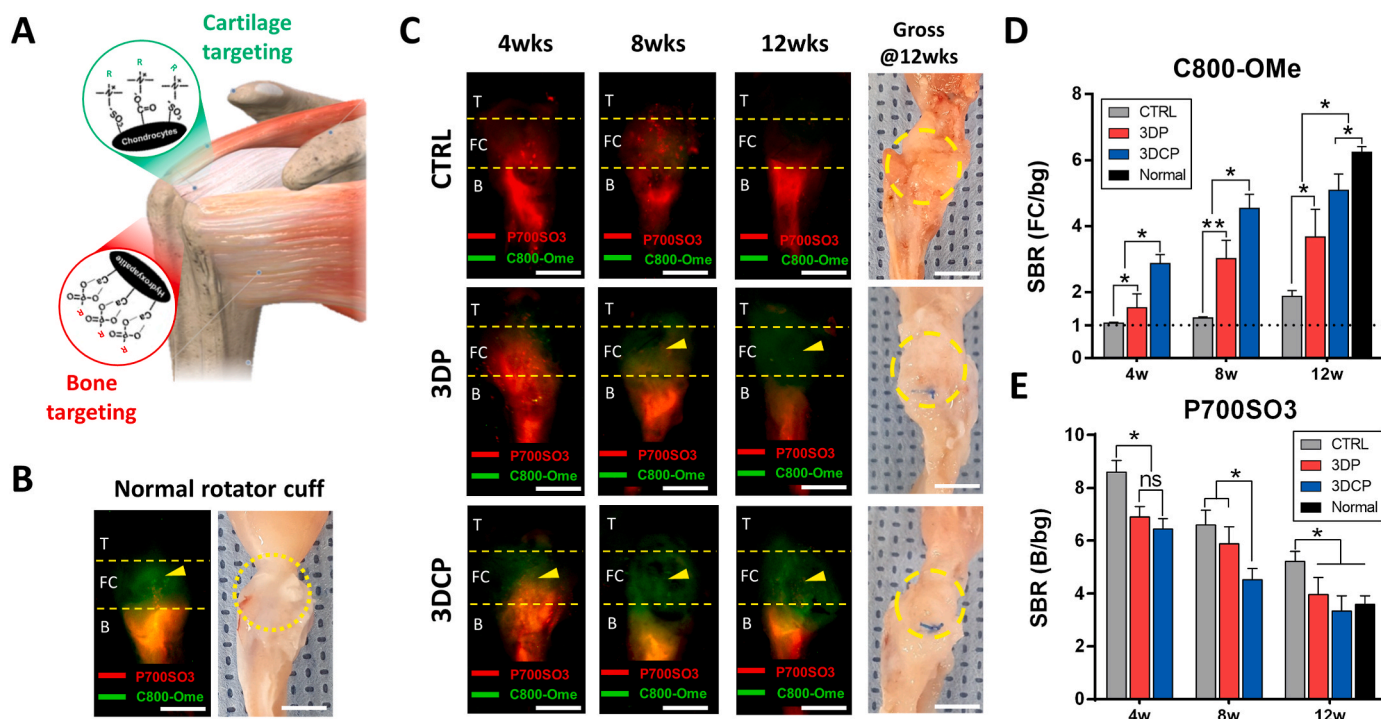


Fig. 6. Assessment of rotator cuff regeneration based on dual-channel NIR imaging. (A) Schematic illustration of cartilage and bone targeting with C800–Ome and P700–SO3, respectively, along with rotator cuff regeneration progression. (B) Dual-channel NIR and color images of normal rat rotator cuff, and (C) repaired rotator cuffs in the CTRL, 3DP, and 3DCP groups at 4, 8, and 12 weeks post-operation. Images were captured at 8 h post-injection of C800–Ome and P700–SO3. Yellow arrowheads indicate new fibrocartilage formation between tendon and bone. Yellow circles indicate the reconstructed rotator cuff at 12 weeks post-operation. Scale bar = 5 mm. (D and E) SBR of (D) C800–Ome in the fibrocartilage phase and (E) P700SO3 in the bone phase at each time point after surgery in the different groups (T: tendon; FC: fibrocartilage; B: bone; bg: background). (n = 6 per group; *p < 0.05 and **p < 0.01; ns: not significant).

against the osteoclast activity during bone resorption and mineral release *in vivo* [37]. Clinically, chronic RC tears can aggravate the bone mineral density of the greater tuberosity with poor bone quality, which may negatively affect the biomechanical properties and lead to high re-tear rate after repair [52]. In the early stages of healing at 4 weeks post-operation, all groups showed wide distribution of P700SO3 and remarkable fluorescence in the greater tuberosity, perhaps owing to the active cortical remodeling process promoted by osteoclast activity. Afterward, 700 nm fluorescence signals in the bone area gradually decreased due to changes in the degree of inflammation and osteoclast density. The 3DP and 3DCP groups both consistently showed similar SBR values of P700SO3 (3DP = 3.9 and 3DCP = 3.3), close to the normal bone tissue level in the late stage of healing at 12 weeks post-operation, while the CTRL group showed a higher SBR and sustained P700SO3 distribution over the entire bone tissues (Fig. 6E). At the final time point of 12 weeks, the gross morphology of the harvested tendon–bone complexes showed complete integration between tendon and bone in the 3DP and 3DCP groups, while a robust fibrovascular scar tissue formation

was observed at TBI in the CTRL group (Fig. 6C). These results consistently demonstrate that the rats in the 3DCP group had a better prognosis in terms of strong fibrocartilage signal and tempered bone resorption activity, reminiscent of the native interface. This non-destructive, consecutive, and tissue-selective NIR imaging approach has several advantages, including visualizing targeted tissue formation in real time, quantifying each fluorescence signal, and minimizing the number of experimental animals required at various timeframes. Overall, dual-channel NIR imaging-based assessment demonstrates the feasibility of visualizing TBI complexes and their structural changes after RC repair and enables quantitative observation of multi-tissue formation, highlighting its diagnostic use for monitoring direct anatomical change and regeneration process in real time.

Following quantitative NIR imaging-based monitoring and its diagnosis for TBI regeneration, we examined the histology with HE, PR, and SO staining at the time of harvesting (12 weeks post-operation) to identify tissue remodeling, multi-tissue formation, and matrix contents of the regenerated TBIs. In response to the above NIR-based imaging

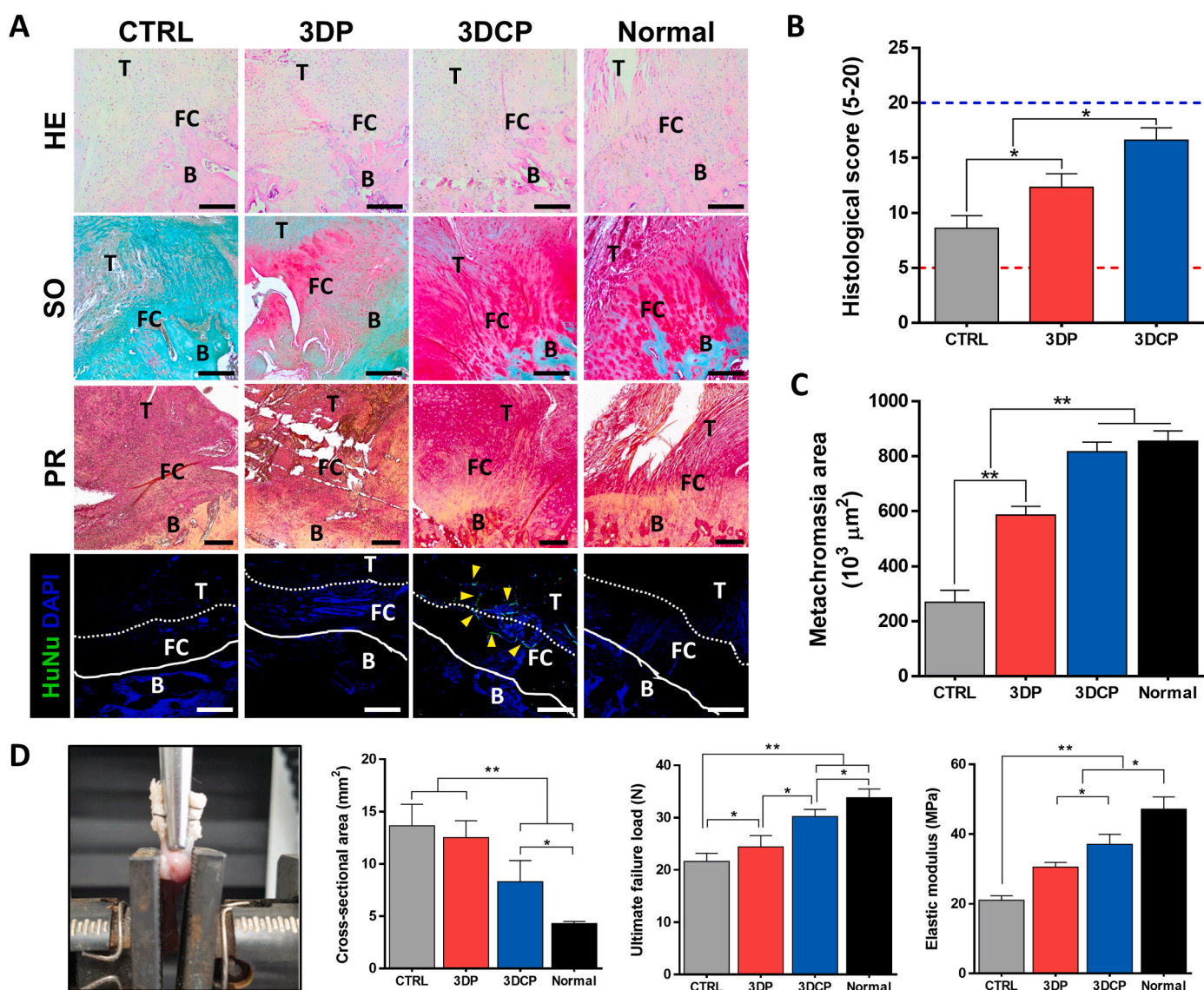


Fig. 7. Representative histological images and mechanical evaluation of repaired rotator cuffs. (A) Hematoxylin–eosin (HE), safranin O (SO), and picosirius red (PR) staining of regenerated TBIs as well as implanted stem cell tracing *in vivo* at 12 weeks post-operation. Scale bar = 200 μm. Yellow arrowheads indicate implanted hBMSCs located near the regenerated fibrocartilage and implantation site. (B) Histological scores of repaired rotator cuffs in the CTRL, 3DP, and 3DCP groups. (C) Comparative analysis of total metachromasia area with SO staining. (T: tendon; FC: fibrocartilage; B: bone). (* $p < 0.05$ and ** $p < 0.01$). (D) Biomechanical evaluation of the regenerated TBI at 12 weeks post-operation. All experiments were performed with $n = 4$ per group. (* $p < 0.05$ and ** $p < 0.01$).

analysis, histological examination demonstrated better repairing effects with the gradient 3DCP cellular scaffold compared with the CTRL and 3DP groups over 12 weeks (Fig. 7A). Histologically, the impaired supraspinatus tendon was firmly reattached to the proximal humerus by a regenerated collagen-rich tissue in all groups at 12 weeks post-operation. The quality of the remodeled fibrocartilage layers at the healing site was better in the 3DP and 3DCP groups than in the CTRL group. Notably, the 3DCP group showed a densely organized collagen structure, proteoglycan-rich fibrocartilage layers with rounded fibrochondrocyte-like cells, and an apparent tidemark making the gradient transition interface more notable, indicating remarkable TBI healing by 3DCP. Because all rats were administrated with an immunosuppressant during the implantation period, we believed that the transplantation of the exogenous human cells into the rats would not trigger a xeno-immune response and the healing process would not be affected. Interestingly, IF staining demonstrated that the implanted hBMMSCs were present near the regenerated fibrocartilage and implantation site, suggesting that the implanted cells survived 12 weeks post-operation in the 3DCP group (Fig. 7A). Quantitatively, the 3DCP group outperformed the other groups, as indicated by higher histological score and greater total metachromasia area for the regenerated fibrocartilage compared to the 3DP and CTRL groups (Fig. 7B and C and Tables S3 and S4). Therefore, repair with 3DCP promoted TBI healing with re-formation of robust fibrocartilaginous transition; these histological assessments were consistent with NIR-based *in vivo* imaging, indicating the reliability of our tissue-targeting NIR imaging system.

The mechanical properties at the TBI are a key indicator to judge the healing quality of the repaired RC as well as the recovery of shoulder function. All specimens from the three groups ruptured at the interface site during the mechanical testing (Fig. 7D). At 12 weeks post-operation, the 3DP and 3DCP groups showed enhanced mechanical outcomes compared with the CTRL group, suggesting a beneficial effect from 3D bioprinted scaffolds on the restoration of mechanical properties following repair. Consistent with the above findings, the mechanical properties of the regenerated TBIs at 12 weeks post-operation in the 3DCP group significantly surpassed those of the CTRL and 3DP groups (Fig. 7D). Notably, the 3DCP group exhibited the lowest cross-sectional area among the experimental groups and had higher ultimate failure load, greater ultimate stress, and larger elastic modulus, with statistically significant differences (Fig. 7D and Table S5). All these results clearly demonstrate that repair with cell-printed implants facilitated mechanical strength improvements at the TBI, which closely approached to those of the normal supraspinatus tendon–bone complex, emphasizing the therapeutic potency of the gradient multi-tissue constructs with cells for functional RC regeneration. Although not addressed at present, investigating dynamic mechanical behaviors (e.g., torsion or cyclic testing) of regenerated TBI will be needed for future work to better understand RC repair stability toward clinical translation.

In the current study, we generated 3D cell-printed constructs with gradient multi-tissue structure for fibrocartilaginous interface regeneration and clarified the regeneration effect of cell-printed constructs in a translational RC tear of a rat model for 12 weeks. The current standard method to determine *in vivo* regenerative efficiency is histological examination which requires the sacrifice of a number of test animals. In a clinical settings, with a strong soft-tissue contrast and multiplanar imaging capabilities, magnetic resonance imaging (MRI) is regarded as an effective diagnostic modality to detect RC tears and provide useful information such as tear degree and tissue quality [53,54]. Despite these merits, MRI has certain disadvantages including high costs, delayed data acquisition, non-continuous operation, and low tissue-specificity, all of which contribute to its inconvenience for real-time intraoperative imaging [54,55]. Alternatively, NIR fluorescence imaging with tissue-specific fluorophores can not only provide accurate and quantitative diagnostic information of RC healing in real time but also reduce the required number of samples or animals over time. This is the first study to validate the RC tear healing effect after repair with cell-printed

implants via tissue-targeting NIR imaging. In this study, we explored the real-time monitoring of multi-tissue regeneration at the implantation site in a rat RC model, which suggesting the translational potential of an NIR-based monitoring system for determining the regenerative ability of 3D cell-printed tissue constructs *in vivo*. Specifically, we compared the therapeutic efficacies of 3DP and 3DCP on TBI healing in the studied rat model. Based on several indicators, including gait analysis, NIR imaging, histology, and mechanical outcomes (Figs. 5–7), our findings comprehensively corroborate that 3DCP implants along with stem cells promote functional TBI healing and mechanical functions, which were significantly better than those of the 3DP and CTRL groups. In the 3DCP group, fibrocartilage-like tissues were moderately observed as early as 4 weeks post-operation, and the regenerated TBIs at 12 weeks had shown integrated fibrocartilaginous transition with gradient structure similar to those of a normal TBI, resulting in improved mechanical strength and restored shoulder locomotion function. It could be logically postulated that after the scaffold was implanted, the exogenous stem cells embedded in gradient multi-tissue constructs would secrete cytokines under the guidance of graded ECM cues that promote recruitment of host endogenous cells and/or direct regional differentiation, leading to early fibrocartilage formation and improved TBI healing; our *in vitro* analyses support our hypothesis to some extent (Figs. 2–4). Consequently, a combination of the gradient multi-tissue construct and stem cells strongly contributed to functional TBI regeneration.

Herein, PU/PCL acted as a template for structural support, offering a mechanically stable environment for the cell-laden bioinks to promote biological activity. Previous studies have reported that PCL scaffolds are often mechanically stiff and may cause friction with the softer native tissue, making them unsuitable for load-bearing applications [56,57]. Thermoplastic PU is another promising material for orthopedic tissue engineering owing its elasticity, tunable physicochemical characteristics, and polymer miscibility. Hence, PU/PCL was selected instead of pure PCL to achieve polymers with intermediate features such as biocompatibility, excellent flexibility, material processability, lower friction property, and adjusted mechanical stiffness for 3D printed implants [58,59]. Owing to the lack of bioactivity, polymeric biomaterials often yield a fibrotic foreign body reaction (FBR) at the biomaterial-host tissue interface, such as inflammation, granulation, fibrosis, and fibrous capsule formation, which hampers the therapeutic efficacy of the biomaterial implants [60]. Once foreign biomaterials are implanted, the FBR is initiated by the host's immunological response, with the spontaneous absorption of blood plasma proteins onto the biomaterial surface and the infiltration and adhesion of the relevant immune cells (e.g., monocytes, neutrophils, giant cells, and macrophages) [61]. However, a severe FBR inevitably results in chronic fibroproliferative responses and fibrous capsule formation that culminate in poor tissue regeneration [62]. We previously demonstrated through subcutaneous murine implantation the *in vivo* biocompatibility of PU/PCL polymeric materials, as observed by the attenuated FBR without collagen-rich scar tissue growth [22]. In agreement with this result, the PU/PCL-based implants utilized in this study did not result in fibrous capsule formation around the implanted polymeric templates at over 12 weeks in a rat model for RC repair.

Our study has a few limitations. First, the lack of characterization of the *in vivo* degradation rate of the implants is a major drawback. Because an ideal scaffold should possess suitable biodegradability during neo-tissue formation, scaffold degradation behavior is one of the critical factors for successful *in vivo* regeneration [12,19]. Despite promoted TBI healing, the implanted PU/PCL synthetic polymers were not completely degraded over the 12-week post-operation period (Fig. S13). In the short-term *in vivo* investigations (12 weeks) conducted in the current study, it was difficult to identify the degradation characteristics of the constructs following *in vivo* implantation. Both PU and PCL have excellent biocompatibility and long-term biostability with a low degradation rate in the order of years [63–65]. Previous literature reported the degradation of PU/PCL-based scaffolds in a biological

environment resulting from a combination of hydrolysis and phagocytosis. The *in vivo* degradation of the scaffold is initiated by the hydrolysis of the PCL segments. The remnant PU segments are phagocytized by macrophages (or giant cells) [66]. It is significant to note that mild acidity typically exists in RC healing. Consequently, the activated neutrophils and macrophages secrete reactive oxygen species and enzymes capable of degrading and eliminating aliphatic PU segments [67]. Thus, complete degradation of the remnant PU/PCL polymeric materials at the implantation site by hydrolysis (PCL segments) and macrophage phagocytosis (PU segments) without a release of toxic products is expected. The degradation also may not elicit chronic inflammation and fibrotic foreign body reaction *in vivo* [25,68]. Given that RC injuries require long-term recovery, incomplete degradation of the polymer can impair the engraftment efficiency and mechanical properties necessary to maintain physiological loads, resulting in the failure of the graft-mediated RC repair [68]. This should be considered in future research to elucidate the *in vivo* degradation profile as well as the long-term stability of the cell-printed constructs. Second, stem cell tracking is another important issue to evaluate the fate of the implanted cells and the treatment efficacy for TBI regeneration, which were not addressed in this study. Future studies are expected to trace the implanted stem cells within the shoulder joint *in vivo* to elucidate their fate and contribution to TBI regeneration *in vivo*. Our systematic *in vivo* study demonstrated that 3DCP constructs along with stem cells revealed native-like TBI formation at the repair site, whereas acellular 3DP constructs showed moderate TBI healing, definitely signifying cell-mediated TBI regeneration. Stem cell-based therapy has shown promising prospects and received enormous attention to treat extensive TBI injuries because implanted stem cells can directly differentiate into targeted lineage and/or have paracrine roles [1,5,9,69]. Previously, NIR fluorescence imaging techniques have been sporadically utilized to study scaffold degradation and stem cell tracking after transplantation of cellular scaffolds *in vivo* [32,34]. We believe that incorporating cell tracking fluorophores with tissue-engineered constructs will allow non-destructive and longitudinal tracking of the grafted exogenous stem cells *in vivo* [70], which could be useful for further identifying cell-mediated TBI formation or regenerative mechanisms over the regeneration period. Third, the underlying mechanisms and key signaling pathways for *in vitro* TBI formation as well as *in vivo* restoration of the gradient TBI structure and functions by the graded ECM cues using TdECM and BdECM bioinks should be clearly identified. In-depth investigations are also required to disclose the interaction between the cell and biomaterial scaffolds, which participate in RC regeneration after implantation *in vivo*. Lastly, the use of primary cells in the 3D cell-printed construct and its *in vivo* application in a large animal model should be realized to investigate the regeneration efficacy of the developed 3D cell-printed TBI constructs for RC repair before clinical trials. Nevertheless, our findings fundamentally highlighted the importance of stem cell-mediated regeneration for graded interface tissue regeneration through the implantation of dECM-based gradient multi-tissue constructs, which has immense potential for future clinical application.

4. Conclusion

In summary, this study demonstrates the functionality of a gradient multi-tissue interface construct for RC regeneration. A 3D cell-printed TBI construct containing inverse gradient of TBI-specific bioinks with stem cells emulated the multi-tissue structure and phenotype mimicking TBI and offered instructive cues for complex interface regeneration in a translational animal model. Tissue-targeting NIR fluorescence-based imaging technology enables not only the visualization of the TBI composite structure of cell-printed constructs *in vitro* but also consecutive monitoring of the *in vivo* regeneration process and multi-tissue formation in real time, allowing for nondestructive prognostic imaging of implanted constructs and their treatment efficacy. Moreover, a 3D cell-

printed implant rapidly and effectively restored shoulder function and promoted TBI healing following RC repair. Overall, we demonstrated the therapeutic contribution of cell-printed constructs in functional RC regeneration, which may open the possibility for their use as regenerative therapy in future clinical practice.

Ethics approval and consent to participate

All animal experiments were approved by Institutional Animal Care and Use Committee of Pohang University of Science and Technology (IACUC number: POSTECH-2021-0008) and were performed according to the guidelines recommended by these committees.

CRediT authorship contribution statement

Suhun Chae: Conceptualization, Methodology, Validation, Formal analysis, Investigation, Writing – original draft, Visualization. **Ujjung Yong:** Methodology, Formal analysis, Investigation, Writing – review & editing, Visualization. **Wonbin Park:** Methodology, Validation, Visualization. **Yoo-mi Choi:** Methodology, Visualization. **In-Ho Jeon:** Conceptualization, Resources. **Homan Kang:** Writing – review & editing. **Jinah Jang:** Resources, Writing – review & editing, Supervision. **Hak Soo Choi:** Conceptualization, Resources, Writing – review & editing, Supervision, Project administration, Funding acquisition. **Dong-Woo Cho:** Conceptualization, Writing – review & editing, Supervision, Project administration, Funding acquisition.

Declaration of competing interest

The authors declare that they have no known competing financial interests or personal relationships that could have appeared to influence the work reported in this paper.

Acknowledgments

The authors would like to thank Chang-Ho Cho, MD from Asan Medical Center for conducting the *in vivo* experiments and rat RC surgeries. This work was supported by the National Research Foundation of Korea (NRF) grant funded by the Korean government (MSIP) (NRF-2020M3H4A1A02084827) (D.-W.C) and the U.S. NIH/NIBIB grants #R01EB022230 (H.S.C.).

Appendix A. Supplementary data

Supplementary data to this article can be found online at <https://doi.org/10.1016/j.bioactmat.2022.05.004>.

References

- [1] Q. Liu, Y. Yu, R.L. Reisdorf, J. Qi, C.-K. Lu, L.J. Berglund, P.C. Amadio, S.L. Moran, S.P. Steinmann, K.-N. An, A. Gingery, C. Zhao, Engineered tendon-fibrocartilage-bone composite and bone marrow-derived mesenchymal stem cell sheet augmentation promotes rotator cuff healing in a non-weight-bearing canine model, *Biomaterials* 192 (2019) 189–198, <https://doi.org/10.1016/j.biomaterials.2018.10.037>.
- [2] S.S. Novakova, V.D. Mahalingam, S.E. Florida, C.L. Mendias, A. Allen, E.M. Arruda, A. Bedi, L.M. Larkin, Tissue-engineered tendon constructs for rotator cuff repair in sheep, *J. Orthop. Res.* 36 (1) (2018) 289–299, <https://doi.org/10.1002/jor.23642>.
- [3] Y. Tang, C. Chen, F. Liu, S. Xie, J. Qu, M. Li, Z. Li, X. Li, Q. Shi, S. Li, X. Li, J. Hu, H. Lu, Structure and ingredient-based biomimetic scaffolds combining with autologous bone marrow-derived mesenchymal stem cell sheets for bone-tendon healing, *Biomaterials* 241 (2020) 119837, <https://doi.org/10.1016/j.biomaterials.2020.119837>.
- [4] B. Chen, Y. Liang, L. Bai, M. Xu, J. Zhang, B. Guo, Z. Yin, Sustained release of magnesium ions mediated by injectable self-healing adhesive hydrogel promotes fibrocartilaginous interface regeneration in the rabbit rotator cuff tear model, *Chem. Eng. J.* 396 (2020) 125335, <https://doi.org/10.1016/j.cej.2020.125335>.
- [5] C. Chen, Y. Chen, M. Li, H. Xiao, Q. Shi, T. Zhang, X. Li, C. Zhao, J. Hu, H. Lu, Functional decellularized fibrocartilaginous matrix graft for rotator cuff entheses regeneration: a novel technique to avoid in-vitro loading of cells, *Biomaterials* 250 (2020) 119996, <https://doi.org/10.1016/j.biomaterials.2020.119996>.

- [6] K.L. Moffat, A.S.P. Kwei, J.P. Spalazzi, S.B. Doty, W.N. Levine, H.H. Lu, Novel nanofiber-based scaffold for rotator cuff repair and augmentation, *Tissue Eng.* 15 (1) (2008) 115–126, <https://doi.org/10.1089/ten.tea.2008.0014>.
- [7] H.K. Min, S.H. Oh, J.M. Lee, G.I. Im, J.H. Lee, Porous membrane with reverse gradients of PDGF-BB and BMP-2 for tendon-to-bone repair: in vitro evaluation on adipose-derived stem cell differentiation, *Acta Biomater.* 10 (3) (2014) 1272–1279, <https://doi.org/10.1016/j.actbio.2013.12.031>.
- [8] C. Zhu, S. Pongkitwitooon, J. Qiu, S. Thomopoulos, Y. Xia, Design and fabrication of a hierarchically structured scaffold for tendon-to-bone repair, *Adv. Mater.* 30 (16) (2018) 1707306, <https://doi.org/10.1002/adma.201707306>.
- [9] D. Wang, X. Zhang, S. Huang, Y. Liu, B.S.-c. Fu, K.K.-I. Mak, A.M. Blocki, P.S.-h. Yung, R.S. Tuan, D.F.E. Ker, Engineering multi-tissue units for regenerative medicine: bone-tendon-muscle units of the rotator cuff, *Biomaterials* 272 (2021) 120789, <https://doi.org/10.1016/j.biomaterials.2021.120789>.
- [10] F. Pittenger Mark, M. Mackay Alastair, C. Beck Stephen, K. Jaiswal Rama, R. Douglas, D. Mosca Joseph, A. Moorman Mark, W. Simonetti Donald, S. Craig, R. Marshak Daniel, Multilineage potential of adult human mesenchymal stem cells, *Science* 284 (5411) (1999) 143–147, <https://doi.org/10.1126/science.284.5411.143>.
- [11] K.W. Liechty, T.C. MacKenzie, A.F. Shaaban, A. Radu, A.B. Moseley, R. Deans, D. R. Marshak, A.W. Flake, Human mesenchymal stem cells engraft and demonstrate site-specific differentiation after in utero transplantation in sheep, *Nat. Med.* 6 (11) (2000) 1282–1286, <https://doi.org/10.1038/81395>.
- [12] Y.-J. Choi, H.-G. Yi, S.-W. Kim, D.-W. Cho, 3D cell printed tissue analogues: a new platform for theranostics, *Theranostics* 7 (12) (2017) 3118–3137, <https://doi.org/10.7150/thno.19396>.
- [13] L.V. Gulotta, D. Kovacevic, J.R. Ehteshami, E. Dagher, J.D. Packer, S.A. Rodeo, Application of bone marrow-derived mesenchymal stem cells in a rotator cuff repair model, *Am. J. Sports Med.* 37 (11) (2009) 2126–2133, <https://doi.org/10.1177/0363546509339582>.
- [14] P. Chen, L. Cui, S.C. Fu, L. Shen, W. Zhang, T. You, T.-Y. Ong, Y. Liu, S.-H. Yung, C. Jiang, The 3D-printed PLGA scaffolds loaded with bone marrow-derived mesenchymal stem cells augment the healing of rotator cuff repair in the rabbits, *Cell Transplant.* 29 (2020), 0963689720973647, <https://doi.org/10.1177/0963689720973647>.
- [15] Y. Huang, B. He, L. Wang, B. Yuan, H. Shu, F. Zhang, L. Sun, Bone marrow mesenchymal stem cell-derived exosomes promote rotator cuff tendon-bone healing by promoting angiogenesis and regulating M1 macrophages in rats, *Stem Cell Res. Ther.* 11 (1) (2020) 496, <https://doi.org/10.1186/s13287-020-02005-x>.
- [16] Y. Zhou, S. Xie, Y. Tang, X. Li, Y. Cao, J. Hu, H. Lu, Effect of book-shaped acellular tendon scaffold with bone marrow mesenchymal stem cells sheets on bone–tendon interface healing, *J. Orthop. Transl.* 26 (2021) 162–170, <https://doi.org/10.1016/j.jot.2020.02.013>.
- [17] J.-H. Yea, T.S. Bae, B.J. Kim, Y.W. Cho, C.H. Jo, Regeneration of the rotator cuff tendon-to-bone interface using umbilical cord-derived mesenchymal stem cells and gradient extracellular matrix scaffolds from adipose tissue in a rat model, *Acta Biomater.* 114 (2020) 104–116, <https://doi.org/10.1016/j.actbio.2020.07.020>.
- [18] H. Mao, L. Yang, H. Zhu, L. Wu, P. Ji, J. Yang, Z. Gu, Recent advances and challenges in materials for 3D bioprinting, *Prog. Nat. Sci.: Mater. Int.* 30 (5) (2020) 618–634, <https://doi.org/10.1016/j.pnsc.2020.09.015>.
- [19] B.S. Kim, S. Das, J. Jang, D.-W. Cho, Decellularized extracellular matrix-based bioinks for engineering tissue- and organ-specific microenvironments, *Chem. Rev.* 120 (19) (2020) 10608–10661, <https://doi.org/10.1021/acs.chemrev.9b00808>.
- [20] F. Pati, J. Jang, D.-H. Ha, S. Won Kim, J.-W. Rhie, J.-H. Shim, D.-H. Kim, D.-W. Cho, Printing three-dimensional tissue analogues with decellularized extracellular matrix bioink, *Nat. Commun.* 5 (1) (2014) 3935, <https://doi.org/10.1038/ncomms4935>.
- [21] J. Jang, H.-J. Park, S.-W. Kim, H. Kim, J.Y. Park, S.J. Na, H.J. Kim, M.N. Park, S. H. Choi, S.H. Park, S.-W. Kim, S.-M. Kwon, P.-J. Kim, D.-W. Cho, 3D printed complex tissue construct using stem cell-laden decellularized extracellular matrix bioinks for cardiac repair, *Biomaterials* 112 (2017) 264–274, <https://doi.org/10.1016/j.biomaterials.2016.10.026>.
- [22] S. Chae, S.-S. Lee, Y.-J. Choi, D.H. Hong, G. Gao, J.H. Wang, D.-W. Cho, 3D cell-printing of biocompatible and functional meniscus constructs using meniscus-derived bioink, *Biomaterials* 267 (2021) 120466, <https://doi.org/10.1016/j.biomaterials.2020.120466>.
- [23] Y.-J. Choi, Y.-J. Jun, D.Y. Kim, H.-G. Yi, S.-H. Chae, J. Kang, J. Lee, G. Gao, J.-S. Kong, J. Jang, W.K. Chung, J.-W. Rhie, D.-W. Cho, A 3D cell printed muscle construct with tissue-derived bioink for the treatment of volumetric muscle loss, *Biomaterials* 206 (2019) 160–169, <https://doi.org/10.1016/j.biomaterials.2019.03.036>.
- [24] G. Gao, H. Kim, B.S. Kim, J.S. Kong, J.Y. Lee, B.W. Park, S. Chae, J. Kim, K. Ban, J. Jang, H.-J. Park, D.-W. Cho, Tissue-engineering of vascular grafts containing endothelium and smooth-muscle using triple-coaxial cell printing, *Appl. Phys. Rev.* 6 (4) (2019), <https://doi.org/10.1063/1.5099306>, 041402.
- [25] S. Chae, Y. Sun, Y.-J. Choi, D.-H. Ha, I. Jeon, D.-W. Cho, 3D cell-printing of tendon-bone interface using tissue-derived extracellular matrix bioinks for chronic rotator cuff repair, *Biofabrication* 13 (3) (2021), <https://doi.org/10.1088/1758-5090/abd159>, 035005.
- [26] A. Prasopthum, Z. Deng, I.M. Khan, Z. Yin, B. Guo, J. Yang, Three dimensional printed degradable and conductive polymer scaffolds promote chondrogenic differentiation of chondroprogenitor cells, *Biomater. Sci.* 8 (15) (2020) 4287–4298, <https://doi.org/10.1039/D0BM00621A>.
- [27] B. Chen, Y. Liang, J. Zhang, L. Bai, M. Xu, Q. Han, X. Han, J. Xiu, M. Li, X. Zhou, B. Guo, Z. Yin, Synergistic enhancement of tendon-to-bone healing via anti-inflammatory and pro-differentiation effects caused by sustained release of Mg²⁺/curcumin from injectable self-healing hydrogels, *Theranostics* 11 (12) (2021) 5911–5925, <https://doi.org/10.7150/thno.56266>.
- [28] B. Guo, P.X. Ma, Synthetic biodegradable functional polymers for tissue engineering: a brief review, *Sci. China Chem.* 57 (4) (2014) 490–500, <https://doi.org/10.1007/s11426-014-5086-y>.
- [29] L.G. Bracaglia, B.T. Smith, E. Watson, N. Arumugasamy, A.G. Mikos, J.P. Fisher, 3D printing for the design and fabrication of polymer-based gradient scaffolds, *Acta Biomater.* 56 (2017) 3–13, <https://doi.org/10.1016/j.actbio.2017.03.030>.
- [30] X. Jiang, S. Wu, M. Kuss, Y. Kong, W. Shi, P.N. Streubel, T. Li, B. Duan, 3D printing of multilayered scaffolds for rotator cuff tendon regeneration, *Bioact. Mater.* 5 (3) (2020) 636–643, <https://doi.org/10.1016/j.bioactmat.2020.04.017>.
- [31] S.Y. Nam, L.M. Ricles, L.J. Suggs, S.Y. Emelianov, Imaging strategies for tissue engineering applications, *Tissue Eng. B Rev.* 21 (1) (2014) 88–102, <https://doi.org/10.1089/ten.teb.2014.0180>.
- [32] S.H. Kim, J.S. Kwon, J.G. Cho, K.G. Park, T.H. Lim, M.S. Kim, H.S. Choi, C.H. Park, S.J. Lee, Non-invasive in vivo monitoring of transplanted stem cells in 3D-bioprinted constructs using near-infrared fluorescent imaging, *Bioeng. & Translat. Med.* 6 (2) (2021), e10216, <https://doi.org/10.1002/btm2.10216>.
- [33] O.F. Vila, M.M. Martino, L. Nebuloni, G. Kuhn, S. Pérez-Amodio, R. Müller, J. A. Hubbell, N. Rubio, J. Blanco, Bioluminescent and micro-computed tomography imaging of bone repair induced by fibrin-binding growth factors, *Acta Biomater.* 10 (10) (2014) 4377–4389, <https://doi.org/10.1016/j.actbio.2014.05.028>.
- [34] S.H. Kim, J.H. Lee, H. Hyun, Y. Ashitate, G. Park, K. Robichaud, E. Lunsford, S. J. Lee, G. Khang, H.S. Choi, Near-infrared fluorescence imaging for noninvasive trafficking of scaffold degradation, *Sci. Rep.* 3 (1) (2013) 1198, <https://doi.org/10.1038/srep01198>.
- [35] L. Jing, M. Sun, P. Xu, K. Yao, J. Yang, X. Wang, H. Liu, M. Sun, Y. Sun, R. Ni, J. Sun, D. Huang, Noninvasive in vivo imaging and monitoring of 3D-printed polycaprolactone scaffolds labeled with an NIR region II fluorescent dye, *ACS Appl. Bio Mater.* 4 (4) (2021) 3189–3202, <https://doi.org/10.1021/acsbio.0c01587>.
- [36] H. Hyun, E.A. Owens, H. Wada, A. Levitz, G. Park, M.H. Park, J.V. Frangioni, M. Henary, H.S. Choi, Cartilage-specific near-infrared fluorophores for biomedical imaging, *Angew. Chem. Int. Ed.* 54 (30) (2015) 8648–8652, <https://doi.org/10.1002/anie.201502287>.
- [37] J.H. Lee, S.Y. Jung, G.K. Park, K. Bao, H. Hyun, G. El Fakhri, H.S. Choi, Fluorometric imaging for early diagnosis and prognosis of rheumatoid arthritis, *Adv. Sci.* 7 (1) (2020) 1902267, <https://doi.org/10.1002/adv.201902267>.
- [38] H. Hyun, H. Wada, K. Bao, J. Gravier, Y. Yadav, M. Laramie, M. Henary, J. V. Frangioni, H.S. Choi, Phosphonated near-infrared fluorophores for biomedical imaging of bone, *Angew. Chem. Int. Ed.* 53 (40) (2014) 10668–10672, <https://doi.org/10.1002/anie.201404930>.
- [39] S. Chae, Y.-J. Choi, D.-W. Cho, Mechanically and biologically promoted cell-laden constructs generated using tissue-specific bioinks for tendon/ligament tissue engineering applications, *Biofabrication* 14 (2) (2022), <https://doi.org/10.1088/1758-5090/ac4fb6>, 025013.
- [40] B.S. Kim, J.-S. Lee, G. Gao, D.-W. Cho, Direct 3D cell-printing of human skin with functional transwell system, *Biofabrication* 9 (2) (2017), <https://doi.org/10.1088/1758-5090/aa71c8>, 025034.
- [41] Y. Liu, S.C. Fu, H.T. Leong, S.K.-K. Ling, J.H. Oh, P.S.-H. Yung, Evaluation of animal models and methods for assessing shoulder function after rotator cuff tear: a systematic review, *J. Orthop. Transl.* 26 (2021) 31–38, <https://doi.org/10.1016/j.jot.2020.02.012>.
- [42] C.-K. Hong, M.-L. Yeh, C.-H. Chang, F.L. Chiang, I.M. Jou, P.-H. Wang, W.-R. Su, Comparison of changes in shoulder functions between biceps tenotomy and tenodesis in an animal model, *Asia-Pacific J. Sports Med. Arthrosc. Rehabil. Technol.* 15 (2019) 17–22, <https://doi.org/10.1016/j.asmart.2018.11.001>.
- [43] Y. Sun, J.-M. Kwak, C. Qi, E. Kholinne, Y. Wang, K.-H. Koh, I.-H. Jeon, Remnant tendon preservation enhances rotator cuff healing: remnant preserving versus removal in a rabbit model, *arthroscopy, J. Arthrosc. & Related Surg.* 36 (7) (2020) 1834–1842, <https://doi.org/10.1016/j.arthro.2020.03.012>.
- [44] P.M. Crapo, T.W. Gilbert, S.F. Badylak, An overview of tissue and whole organ decellularization processes, *Biomaterials* 32 (12) (2011) 3233–3243, <https://doi.org/10.1016/j.biomaterials.2011.01.057>.
- [45] M. Wu, G. Chen, Y.-P. Li, TGF- β and BMP signaling in osteoblast, skeletal development, and bone formation, homeostasis and disease, *Bone Res.* 4 (1) (2016) 16009, <https://doi.org/10.1038/boneres.2016.9>.
- [46] S. Shahab-Osterloh, F. Witte, A. Hoffmann, A. Winkel, S. Laggies, B. Neumann, V. Seiffart, W. Lindenmaier, A.D. Gruber, J. Ringe, T. Häupl, F. Thorey, E. Willbold, P. Corbeau, G. Gross, Mesenchymal stem cell-dependent formation of heterotopic tendon-bone insertions (osteotendinous junctions), *Stem Cell.* 28 (9) (2010) 1590–1601, <https://doi.org/10.1002/stem.487>.
- [47] R.C. Locke, A.C. Abraham, M.L. Killian, Orthopedic interface repair strategies based on native structural and mechanical features of the multiscale enthesis, *ACS Biomater. Sci. Eng.* 3 (11) (2017) 2633–2643, <https://doi.org/10.1021/acsbomaterials.6b00599>.
- [48] Y. Sugimoto, A. Takimoto, H. Akiyama, R. Kist, G. Scherer, T. Nakamura, Y. Hiraki, C. Shukunami, Sox+ / Sox9+ progenitors contribute to the establishment of the junction between cartilage and tendon/ligament, *Development* 140 (11) (2013) 2280–2288, <https://doi.org/10.1242/dev.096354>.
- [49] S. Eyal, S. Kult, S. Rubin, S. Krief, N. Felsenthal, K.M. Pineault, D. Leshkowitz, T.-M. Salame, Y. Addadi, D.M. Wellik, E. Zelzer, Bone morphology is regulated modularly by global and regional genetic programs, *Development* 146 (14) (2019), <https://doi.org/10.1242/dev.167882>.
- [50] A.G. Schwartz, L.M. Galatz, S. Thomopoulos, Enthesis regeneration: a role for Gli1 + progenitor cells, *Development* 144 (7) (2017) 1159–1164, <https://doi.org/10.1242/dev.139303>.

- [51] N.A. Dymont, A.P. Breidenbach, A.G. Schwartz, R.P. Russell, L. Aschbacher-Smith, H. Liu, Y. Hagiwara, R. Jiang, S. Thomopoulos, D.L. Butler, D.W. Rowe, Gdf5 progenitors give rise to fibrocartilage cells that mineralize via hedgehog signaling to form the zonal enthesis, *Dev. Biol.* 405 (1) (2015) 96–107, <https://doi.org/10.1016/j.ydbio.2015.06.020>.
- [52] V. Entezari, M. Lazarus, Surgical considerations in managing osteoporosis, osteopenia, and vitamin D deficiency during arthroscopic rotator cuff repair, *Orthop. Clin. N. Am.* 50 (2) (2019) 233–243, <https://doi.org/10.1016/j.ocl.2018.10.006>.
- [53] J.-H. Kim, J.-W. Park, S.-Y. Heo, Y.-M. Noh, Magnetic resonance imaging analysis of rotator cuff tear after shoulder dislocation in a patient older than 40 years, *Clin. Shoulder Elbow* 23 (3) (2020) 144–151, <https://doi.org/10.5397/cise.2020.00227>.
- [54] S.B. Gururaj Sharma, Ganesh Khandige, Utkarsh Kabra, MR imaging of rotator cuff tears: correlation with arthroscopy, *J. Clin. Diagn. Res.* 11 (5) (2017) TC24–TC27, <https://doi.org/10.7860/JCDR/2017/27714.9911>.
- [55] E.A. Owens, M. Henary, G. El Fakhri, H.S. Choi, Tissue-specific near-infrared fluorescence imaging, *Accounts Chem. Res.* 49 (9) (2016) 1731–1740, <https://doi.org/10.1021/acs.accounts.6b00239>.
- [56] E. Cipriani, P. Bracco, S.M. Kurtz, L. Costa, M. Zanetti, In-vivo degradation of poly (carbonate-urethane) based spine implants, *Polym. Degrad. Stabil.* 98 (6) (2013) 1225–1235, <https://doi.org/10.1016/j.polymdegradstab.2013.03.005>.
- [57] G. Bahcecioglu, B. Bilgen, N. Hasirci, V. Hasirci, Anatomical meniscus construct with zone specific biochemical composition and structural organization, *Biomaterials* 218 (2019) 119361, <https://doi.org/10.1016/j.biomaterials.2019.119361>.
- [58] A.O. Inyang, C.L. Vaughan, Functional characteristics and mechanical performance of PCU composites for knee meniscus replacement, *Materials* 13 (8) (2020) 1886, <https://doi.org/10.3390/ma13081886>.
- [59] M.A. Woodruff, D.W. Hutmacher, The return of a forgotten polymer—polycaprolactone in the 21st century, *Prog. Polym. Sci.* 35 (10) (2010) 1217–1256, <https://doi.org/10.1016/j.progpolymsci.2010.04.002>.
- [60] J.M. Anderson, Exploiting the inflammatory response on biomaterials research and development, *J. Mater. Sci. Mater. Med.* 26 (3) (2015) 121, <https://doi.org/10.1007/s10856-015-5423-5>.
- [61] M. Deng, J. Tan, C. Hu, T. Hou, W. Peng, J. Liu, B. Yu, Q. Dai, J. Zhou, Y. Yang, R. Dong, C. Ruan, S. Dong, J. Xu, Modification of PLGA scaffold by MSC-derived extracellular matrix combats macrophage inflammation to initiate bone regeneration via TGF- β -induced protein, *Adv. Healthc. Mater.* 9 (13) (2020) 2000353, <https://doi.org/10.1002/adhm.202000353>.
- [62] J.L. Hernandez, J. Park, S. Yao, A.K. Blakney, H.V. Nguyen, B.H. Katz, J.T. Jensen, K.A. Woodrow, Effect of tissue microenvironment on fibrous capsule formation to biomaterial-coated implants, *Biomaterials* 273 (2021) 120806, <https://doi.org/10.1016/j.biomaterials.2021.120806>.
- [63] G.A. Skarja, K.A. Woodhouse, In vitro degradation and erosion of degradable, segmented polyurethanes containing an amino acid-based chain extender, *J. Biomater. Sci. Polym. Ed.* 12 (8) (2001) 851–873, <https://doi.org/10.1163/156856201753113060>.
- [64] J.D. Fromstein, K.A. Woodhouse, Elastomeric biodegradable polyurethane blends for soft tissue applications, *J. Biomater. Sci. Polym. Ed.* 13 (4) (2002) 391–406, <https://doi.org/10.1163/156856202320253929>.
- [65] J.H. Ashton, J.A.M. Mertz, J.L. Harper, M.J. Slepian, J.L. Mills, D.V. McGrath, J. P. Vande Geest, Polymeric endoarterial paving: mechanical, thermoforming, and degradation properties of polycaprolactone/polyurethane blends for cardiovascular applications, *Acta Biomater.* 7 (1) (2011) 287–294, <https://doi.org/10.1016/j.actbio.2010.09.004>.
- [66] J. de Groot, Actifit, Polyurethane meniscus implant: basic science, in: P. Beaufils, R. Verdonk (Eds.), *The Meniscus*, Springer Berlin Heidelberg, Berlin, Heidelberg, 2010, pp. 383–387.
- [67] S. Mohajeri, B.G. Amsden, In vivo degradation mechanism and biocompatibility of a biodegradable aliphatic polycarbonate: poly(trimethylene carbonate-co-5-hydroxy trimethylene carbonate), *ACS Appl. Bio Mater.* 4 (4) (2021) 3686–3696, <https://doi.org/10.1021/acsabm.1c00160>.
- [68] D.F.E. Ker, D. Wang, A.W. Behn, E.T.H. Wang, X. Zhang, B.Y. Zhou, Á.E. Mercado-Pagán, S. Kim, J. Kleimeyer, B. Gharaibeh, Y. Shanjani, D. Nelson, M. Safran, E. Cheung, P. Campbell, Y.P. Yang, Functionally graded, bone- and tendon-like polyurethane for rotator cuff repair, *Adv. Funct. Mater.* 28 (20) (2018) 1707107, <https://doi.org/10.1002/adfm.201707107>.
- [69] Y. Zhang, T. Lei, C. Tang, Y. Chen, Y. Liao, W. Ju, H. Zhang, B. Zhou, R. Liang, T. Zhang, C. Fan, X. Chen, Y. Zhao, Y. Xie, J. Ye, B.C. Heng, X. Chen, Y. Hong, W. Shen, Z. Yin, 3D printing of chemical-empowered tendon stem/progenitor cells for functional tissue repair, *Biomaterials* 271 (2021) 120722, <https://doi.org/10.1016/j.biomaterials.2021.120722>.
- [70] G.K. Park, J.H. Lee, A. Levitz, G. El Fakhri, N.S. Hwang, M. Henary, H.S. Choi, Lysosome-targeted bioprobes for sequential cell tracking from macroscopic to microscopic scales, *Adv. Mater.* 31 (14) (2019) 1806216, <https://doi.org/10.1002/adma.201806216>.